SIAM J. IMAGING SCIENCES
Vol. 17, No. 1, pp. 415–440
© 2024 Society for Industrial and Applied Mathematics

Analysis of View Aliasing for the Generalized Radon Transform in $\mathbb{R}^2$*

Alexander Katsevich†

Abstract. In this paper we consider the generalized Radon transform $\mathcal{R}$ in the plane. Let f be a piecewise smooth function, which has a jump across a smooth curve $\mathcal{S}$. We obtain a formula, which accurately describes view aliasing artifacts away from $\mathcal{S}$ when f is reconstructed from the data $\mathcal{R}f$ discretized in the view direction. The formula is asymptotic, it is established in the limit as the sampling rate $\epsilon \to 0$. The proposed approach does not require that f be band-limited. Numerical experiments with the classical Radon transform and generalized Radon transform (which integrates over circles) demonstrate the accuracy of the formula.

Key words. aliasing, generalized Radon, reconstruction, asymptotic estimates

MSC codes. 44A12, 94A20, 92C55, 94A12

DOI. 10.1137/23M1554746

1. Introduction.

Resolution of image reconstruction from discrete data is one of the fundamental questions in imaging. The most direct approach to estimating resolution utilizes the notions of the point spread function and modulation transfer function [1, sections 12.2, 12.3]. This and other similar approaches allow rigorous theoretical analysis of only the simplest settings, such as inversion of the classical Radon transform. For the most part, resolution of reconstruction in more difficult settings (e.g., inversion of the cone beam transform) is analyzed by heuristic arguments, numerically, or via measurements [2, 3, 4].

Sampling theory provides a related approach to investigating resolution [5, 6, 7, 8, 9, 10, 11, 12, 13, 14]. Consider, for example, the classical Radon transform in $\mathbb{R}^2$

$$\hat{f}(\alpha,p)=\int_{\mathbb{R}^2} f(x)\delta(\vec{\alpha}\cdot x-p)\mathrm{d}x,\ \ \vec{\alpha}=(\cos\alpha,\sin\alpha). \tag{1.1}$$

The corresponding discrete data are

$$\hat{f}(\alpha_k,p_j),\ \ \alpha_k=\bar{\alpha}+k\Delta\alpha,\ \ p_j=\bar{p}+j\Delta p,\ \ \alpha_k\in[0,2\pi),\ j\in\mathbb{Z}, \tag{1.2}$$

for some fixed $\bar{\alpha}$, $\bar{p}$ and $\Delta\alpha$, Δp. Assume that f is essentially band limited (in the classical sense). This means that, with high accuracy, its Fourier transform $\tilde{f}(\xi)$ is supported in some ball $|\xi|\le B$. The sampling theory predicts the rates $\Delta\alpha$, Δp with which $\hat{f}(\alpha,p)$ should be

*Received by the editors February 21, 2023; accepted for publication (in revised form) October 31, 2023; published electronically February 23, 2024.
https://doi.org/10.1137/23M1554746
Funding: The work of the author was partially supported by the National Science Foundation grant DMS-1906361.
†Department of Mathematics, University of Central Florida, Orlando, FL 32816-1364 USA (alexander.katsevich@ucf.edu).

Copyright © by SIAM. Unauthorized reproduction of this article is prohibited.

Downloaded 09/12/24 to 5.198.137.25 . Redistribution subject to SIAM license or copyright; see https://epubs.siam.org/terms-privacy

sampled, so that reconstruction of f from discrete data does not contain aliasing artifacts. Since the essential band-limit B is related to the size of the smallest detail in f, a typical prescription of the theory can be loosely formulated as follows: given the size of the smallest detail in f, the minimal sampling rates to avoid aliasing are $\Delta\alpha$, Δp. Alternatively, the theory determines the size of the smallest detail in f that can be resolved given the rates $\Delta\alpha$, Δp.

A microlocal approach to sampling was developed recently [15, 16, 17]. In this approach f is assumed to be band-limited in the semiclassical sense (i.e., the semiclassical wavefront set $\mathrm{WF}_h(f)$ is compact). Alternatively, the assumption is that the data represent discrete values of the convolution $w * \mathcal{R}f$. Here $\mathcal{R}$ is the generalized Radon transform, and w is a semiclassically band-limited mollifier. The mollifier models the detector aperture function. The goal is to accurately recover the semiclassical singularities of f and avoid aliasing. If the sampling requirement is violated, the theory predicts the location and frequency of aliasing artifacts.

In [18, 19, 20, 21, 22], the author developed an alternative analysis of resolution (we call it local resolution analysis, or LRA). The main results in these papers are simple expressions describing the reconstruction from discrete values of $\mathcal{R}f$ or $w * \mathcal{R}f$ in a neighborhood of the singularities of f in a variety of settings. We call these expressions the discrete transition behavior (DTB). DTB provides a direct, quantitative link between the sampling rate and resolution. In these papers such a link is established for a wide range of integral transforms, conormal distributions f, and reconstruction operators. In [23, 24] LRA was generalized to objects with rough boundaries in $\mathbb{R}^2$. Neither f nor the mollifier w (if applied) is required to be band-limited.

Suppose $\Delta p = \epsilon$ and $\Delta\alpha = \kappa\epsilon$, where $\kappa > 0$ is fixed. The DTB is an accurate approximation of the reconstruction in an ϵ-neighborhood of the singular support of f in the limit as $\epsilon \to 0$. Therefore, the DTB provides much more than a single measure of resolution (e.g., the size of the smallest detail that can be resolved). Given the DTB function, the user may decide in a fully quantitative way what sampling rate is required to achieve a user-defined reconstruction quality. The notion of quality may include resolution (which can be described in any desired way) and/or any other requirement the user desires. Thus, the LRA answers precisely the question of the required sampling rate to guarantee the required resolution (understood broadly).

The only item missing from the LRA until now was analysis of aliasing. Some earlier results on the analysis of aliasing artifacts (more precisely, view aliasing artifacts) are in [24] and [1, Section 12.3.2]. They include an approximate formula for the artifacts far from a small, radially symmetric object. More recent results are in [15, 16, 17]. These include the prediction of the location and frequency of the artifacts, qualitative analysis of the artifacts generated by various edges (e.g., flat, convex and a corner), as well as their numerical illustrations.

In this paper we generalize the LRA to the analysis of view aliasing. We call it the Localized Aliasing Analysis, or LAA. Our main result is Theorem 2.5, where a precise, quantitative formula describing aliasing artifacts is stated. The formula is asymptotic; it is established in the limit as the sampling rate $\epsilon \to 0$ (which is the same assumption as in [15, 16, 17]). Similarly to the LRA, the LAA is very flexible. In this paper we consider the generalized Radon transform in $\mathbb{R}^2$ and apply it to functions with jump discontinuities across smooth curves. Similarly to [18, 19, 20, 21, 22], we believe that the LAA is generalizable, and that

Downloaded 09/12/24 to 5.198.137.25 . Redistribution subject to SIAM license or copyright; see https://epubs.siam.org/terms-privacy

Copyright © by SIAM. Unauthorized reproduction of this article is prohibited.

Downloaded 09/12/24 to 5.198.137.25 . Redistribution subject to SIAM license or copyright; see https://epubs.siam.org/terms-privacy

it is capable of predicting aliasing artifacts for a wide range of integral transforms, conormal distributions f, and reconstruction operators.

To avoid confusion, we clarify the meaning of the terms "resolution" and "aliasing" used in this paper. For simplicity, we will use the example of a jump discontinuity across a smooth curve $\mathcal{S}$. Resolution at $x_0 \in \mathcal{S}$ means the extent to which the boundary at the jump (i.e., $\mathcal{S}$) is blurred when the image is reconstructed in a neighborhood of x_0 from discrete data. This blurring is accurately described by the DTB function mentioned above. The derivation of the DTB function accounts for possible artifacts that may arise due to aliasing from the parts of $\mathcal{S}$ in a neighborhood of x_0. In other words, *LRA treats local aliasing as part of resolution analysis.* In this paper, the term *aliasing stands for rapidly oscillating artifacts away from* $\mathcal{S}$ *that are caused by aliasing from* $\mathcal{S}$.

The paper is organized as follows. In section 2 we describe the set-up, formulate assumptions, and state the main result—Theorem 2.5. This theorem provides a simple formula that describes aliasing artifacts. We also discuss various quantities used in the formula and state a corollary that describes what the formula looks like in the case of the classical Radon transform. The proof of Theorem 2.5 is in section 3. Section 4.1 establishes a few useful properties of the function Ψ, in terms of which the artifacts are described. An algorithm for computing Ψ numerically is in section 4.2. Section 5 contains numerical experiments with the classical and generalized Radon transforms. The latter integrates over circles. Details of implementation, which illustrate the use of the theorem, are provided. All experiments demonstrate a good match between reconstruction and prediction. Proofs of some lemmas are in Appendix A.

2. Preliminaries.

2.1. Generalized Radon transform.

Let $p = \mathcal{P}_*(\alpha, x)$ be a defining function for the generalized Radon transform $\mathcal{R}$:

$$\hat{f}(\alpha, p) = \int_{\mathcal{S}_{\alpha,p}} W(\alpha, p; x) f(x) \mathrm{d}A, \ \mathcal{S}_{\alpha,p} := \{x \in \mathbb{R}^2 : \mathcal{P}_*(\alpha, x) = p\}, \alpha \in \Omega, \ p \in \mathbb{R}, \tag{2.1}$$

where $W \in C^\infty(\Omega \times \mathbb{R} \times U)$ is some (known) integration weight, $\mathrm{d}A$ is the length element on the curve $\mathcal{S}_{\alpha,p}$, $U \subset \mathbb{R}^2$ is a small open set, and $\Omega \subset \mathbb{R}$ is a small interval. Similarly to the classical Radon transform, we think of α as the polar angle, and p as the affine variable. However, since we consider the generalized Radon transform, these variables admit many alternative interpretations. See [25, 26] for more information and references about generalized Radon transforms, their properties, and applications.

Let $\mathcal{S}$ be a C^∞ curve. Let $(\alpha_\star, p_\star)$ be a pair such that $\mathcal{S}_{\alpha_\star,p_\star}$ is tangent to $\mathcal{S}$ at some $y_0 \in \mathcal{S} \cap U$. To simplify notation, denote $\mathcal{S}_\star := \mathcal{S}_{\alpha_\star,p_\star}$. We will compute a reconstruction in a small neighborhood of some point $x_0 \notin \mathcal{S}$. Let $H(y) = 0$ be an equation for $\mathcal{S}$ in a neighborhood of y_0. The function H is smooth and $\mathrm{d}H(y) \neq 0$, $y \in \mathcal{S}$. Multiplying H by a constant if necessary, we can assume that $\mathcal{P}_*$ satisfies the equations

$$\mathcal{P}_*(\alpha_\star, x_0) = \mathcal{P}_*(\alpha_\star, y_0) = p_\star, \ \mathrm{d}_x \mathcal{P}_*(\alpha_\star, y_0) = \mathrm{d}H(y_0). \tag{2.2}$$

Assumption 2.1 (properties of $\mathcal{P}_*$).

1. $\mathcal{P}_* \in C^\infty(\Omega \times U)$ and $\mathrm{d}_x \mathcal{P}_*(\alpha, x) \neq 0$, $x = x_0, y_0$.

Copyright © by SIAM. Unauthorized reproduction of this article is prohibited.

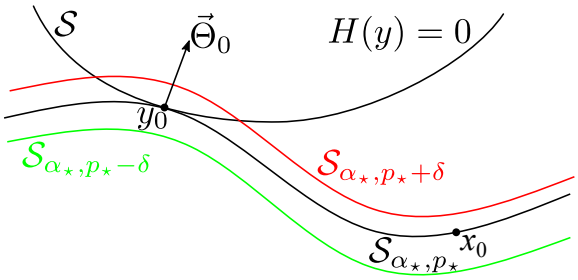

Figure 1. *Illustration of the curves $\mathcal{S}$ and $\mathcal{S}_{\alpha,p}$.*

2. Equations (2.2) hold.
3. $\partial_\alpha \mathcal{P}_*(\alpha_\star, x_0) \neq \partial_\alpha \mathcal{P}_*(\alpha_\star, y_0)$ (the Bolker condition).
4. One has

$$M := (\vec{\Theta}_0^{\perp} \cdot \partial_y)^2 (\mathcal{P}_*(\alpha_\star, y) - H(y))|_{y=y_0} > 0, \tag{2.3}$$

   where $\vec{\Theta}_0^{\perp}$ is a unit vector orthogonal to $\mathrm{d}H(y_0)$.
5. There exists $c > 0$ such that $y_0 \notin \mathcal{S}_{\alpha,p}$ for any $\alpha \in \Omega$ and $|p - p_\star| \geq c$.

Assumption 2.1(4) is equivalent to the condition that the curvatures of $\mathcal{S}$ and $\mathcal{S}_\star$ at y_0 are not equal. In other words, the order of contact between $\mathcal{S}$ and $\mathcal{S}_\star$ is one (and not higher). For example, if one of the two curves is flat at y_0, then $M \neq 0$ as long as the other one is not flat. The requirement that M be positive is not restrictive. If $M < 0$, we can flip the p-axis and replace $H \to -H$, $\mathcal{P}_* \to -\mathcal{P}_*$ to make M positive. The essential requirement is that $M \neq 0$.

The requirement $M > 0$ means that $\mathcal{S}_{\alpha_\star,p_\star+\delta}$ intersects $\mathcal{S}$ at two points near y_0 when $\delta > 0$, and does not intersect $\mathcal{S}$ near y_0 if $\delta < 0$ (see Figure 1). In what follows we set

$$\vec{\Theta}_0 := \pm \mathrm{d}H(y_0), \tag{2.4}$$

and the sign (+ or −) is selected so that $\vec{\Theta}_0$ points towards the part of $\mathcal{S}_{\alpha_\star,p_\star+\delta}$, $0 < \delta \ll 1$, located between its two intersection points with $\mathcal{S}$ (see Figure 1).

Shrinking, if necessary, Ω and U further, we may assume that there is no other pair $(\alpha', p') \neq (\alpha_\star, p_\star)$, $\alpha' \in \Omega$, such that $x_0 \in \mathcal{S}_{\alpha',p'}$ and $\mathcal{S}_{\alpha',p'}$ is tangent to $\mathcal{S}$ at y_0.

Let $\mathcal{P}(\alpha)$, $\alpha \in \Omega$, be the function defined by the requirement that the curves $\mathcal{S}_{\alpha,\mathcal{P}(\alpha)}$ be tangent to $\mathcal{S}$ in a neighborhood of y_0. Figure 2 illustrates the function $\mathcal{P}(\alpha)$ in the case of the classical Radon transform (left panel) and the generalized Radon transform that integrates over circles (right panel). The circles have arbitrary radii and centers on a given curve $z(\alpha) \in \Gamma$, $\alpha \in \Omega$. Consider the latter case. Suppose, for example, that $\mathcal{S}$ is a circle with radius r and center a. Then, globally, there are two such functions: $\mathcal{P}(\alpha) = |z(\alpha) - a| \pm r$. See also section 5.2 for more details about the circular Radon transform.

The following simple lemma is proven in Appendix A.1.

Lemma 2.2. *For a sufficiently small neighborhood $\Omega \ni \alpha_\star$, one has*

$$\mathcal{P}(\alpha_\star) = p_\star, \ \mathcal{P}(\alpha) \in C^\infty(\Omega), \ \partial_\alpha \mathcal{P}_*(\alpha_\star, y_0) = \mathcal{P}'(\alpha_\star). \tag{2.5}$$

Downloaded 09/12/24 to 5.198.137.25 . Redistribution subject to SIAM license or copyright; see https://epubs.siam.org/terms-privacy

Copyright © by SIAM. Unauthorized reproduction of this article is prohibited.

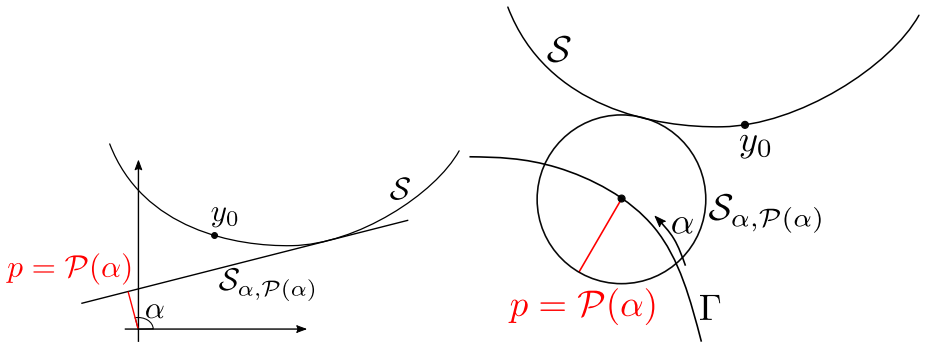

Figure 2. *Illustration of the function $\mathcal{P}(\alpha)$. Left panel: the classical Radon transform that integrates over lines. Right panel: the generalized Radon transform that integrates over circles with centers on a given curve parametrized by α (denoted Γ in the figure).*

From Assumptions 2.1(1), 2.1(3) and Lemma 2.2,

$$u_0 := \mathrm{d}_x \mathcal{P}_*(\alpha_\star, x_0) \neq 0,\ \ \mu_0 := \partial_\alpha(\mathcal{P}_*(\alpha_\star, x_0) - \mathcal{P}(\alpha_\star)) \neq 0. \tag{2.6}$$

2.2. Remaining assumptions and main result. Consider a function $f(x)$ on the plane, $x \in \mathbb{R}^2$. We suppose the following.

Assumption 2.3 (properties of f).

1. $\operatorname{supp}(f) \subset U$ and $\operatorname{diam}(U)$ is sufficiently small.
2. There exist open sets $D_\pm$ and functions $f_\pm \in C^\infty(\mathbb{R}^2)$ such that

$$\begin{aligned} &f(x) \equiv f_-(x),\ x \in D_-,\ \ f(x) \equiv f_+(x),\ x \in D_+, \\ &D_- \cap D_+ = \varnothing,\ \ D_- \cup D_+ = U \setminus \mathcal{S}, \end{aligned} \tag{2.7}$$

3. $\mathcal{S} \cap U$ is a C^∞ curve.

Thus, $\operatorname{sing\,supp}(f) \subset \mathcal{S}$. In general, $f_-(x) \neq f_+(x)$, $x \in \mathcal{S}$, so f may have a jump across $\mathcal{S}$. Note that whether $x_0 \in U$ or not is irrelevant. Also, when U shrinks towards y_0, $\mathcal{S}$ does not change. Thus, $\mathcal{S} \cap U$ is a small segment of $\mathcal{S}$ around y_0. With this understanding, in what follows we do not distinguish between $\mathcal{S}$ and $\mathcal{S} \cap U$.

Similarly to [17], we consider semidiscrete data

$$\hat{f}_\epsilon(\alpha_k, p) := \int w_\epsilon(p - s)\hat{f}(\alpha_k, s)\mathrm{d}s,\ \ \alpha_k := k\Delta\alpha,\ \ p \in \mathbb{R},\ \ w_\epsilon(t) := \epsilon^{-1} w(t/\epsilon), \tag{2.8}$$

where w is a mollifier (e.g., the detector aperture function), $\Delta\alpha = \kappa\epsilon$, and $\kappa > 0$ is fixed. It is reasonable to assume that the support of w_ϵ is of size $O(\epsilon)$, because sampling rates along α and p are usually of the same order of magnitude.

Assumption 2.4 (assumptions about the mollifier w).

1. w is compactly supported and $w' \in L^q(\mathbb{R})$ for some $q > 2$ and
2. $\int w(p)\mathrm{d}p = 1$.

Copyright © by SIAM. Unauthorized reproduction of this article is prohibited.

Downloaded 09/12/24 to 5.198.137.25 . Redistribution subject to SIAM license or copyright; see https://epubs.siam.org/terms-privacy

Hence, the data (2.8) represent the integrals of f along thin strips around $\mathcal{S}_{\alpha_k,p}$, and their width ($=O(\epsilon)$) is determined by ϵ and the support of w. In the ideal case (not considered in this paper), where w is the Dirac δ-function, the data represent the integrals of f along $\mathcal{S}_{\alpha_k,p}$.

Reconstruction from the data (2.8) is achieved by the formula

$$f_\epsilon^{\text{rec}}(x) = -\frac{\Delta\alpha}{2\pi}\sum_{\alpha_k\in\Omega}\frac{\omega(\alpha_k,x)}{\pi}\int\frac{\partial_p\hat{f}_\epsilon(\alpha_k,p)}{p-\mathcal{P}_*(\alpha_k,x)}\mathrm{d}p,\ x\in U', \tag{2.9}$$

where U' is a small neighborhood of x_0 and $\omega\in C^\infty(\Omega\times U')$ is some weight function. This is a discretized (in α) version of the classical filtered back-projection inversion formula [27] adapted to the generalized Radon transform in $\mathbb{R}^2$ (e.g., as it was done in [28, 29]). The integral with respect to p, which is understood in the principal value sense, is the filtering step (the Hilbert transform). The exterior sum is a quadrature rule corresponding to the backprojection integral.

To better understand (2.9), we consider its continuous analogue. Suppose w is the δ-function. The continuous version of (2.9) reads

$$f^{\text{rec}} = \mathcal{R}^*(\mathcal{H}\partial_p)\mathcal{R}f. \tag{2.10}$$

Here $\mathcal{R}^*$ is a weighted adjoint transform and $\mathcal{H}$ is the Hilbert transform acting with respect to p. By imposing additional restrictions on $\mathcal{P}_*$, ω, and W we can ensure that $\mathcal{R}^*(\mathcal{H}\partial_p)\mathcal{R}$ is a ΨDO of order zero (see, e.g., [28, 30]) with some other desired properties (e.g., elliptic, principal symbol equal 1). We do not do this, since our focus here is only the reconstruction of rapidly oscillating artifacts in f_ϵ^{rec} away from $\mathcal{S}$. In particular, no attempt is made to achieve exact reconstruction. In view of this we impose only a minimal set of conditions that guarantee that Theorem 2.5 holds. These conditions do not guarantee that $\mathcal{R}^*(\mathcal{H}\partial_p)\mathcal{R}$ is a ΨDO.

Introduce the following functions:

$$\begin{aligned}
&\psi(\hat{q}) := (1/2)\int_0^\infty w(\hat{q}+\hat{p})\hat{p}^{-1/2}\mathrm{d}\hat{p},\ \hat{q}\in\mathbb{R},\\
&\Psi(h;a,r) := \sum_{k\in\mathbb{Z}}\left[\psi\left(a(k-r)+h\right)-\psi\left(a(k-r)\right)\right],\ h,a,r\in\mathbb{R}, a\neq 0,\\
&\Psi(h;0,r) := 0,\ h,r\in\mathbb{R},
\end{aligned} \tag{2.11}$$

and

$$\Delta f(y_0) = \lim_{\epsilon\to 0^+}\left(f(y_0+\epsilon\vec{\Theta}_0)-f(y_0-\epsilon\vec{\Theta}_0)\right). \tag{2.12}$$

Various properties of ψ and Ψ (e.g., that ψ is continuous and decays sufficiently fast, so that the series in the definition of Ψ is absolutely convergent) are established in sections 3.1 and 4. Our main result is as follows.

Theorem 2.5. *Suppose $W\in C^\infty(\Omega\times\mathbb{R}\times U)$ and $\omega\in C^\infty(\Omega\times U')$ for some small open sets $\Omega\ni\alpha_\star$, $U\ni y_0$, and $U'\ni x_0$. Under Assumptions 2.1, 2.3, and 2.4, one has*

$$\begin{aligned}
&\epsilon^{-1/2}(f_\epsilon^{rec}(x_0+\epsilon\check{x})-f_\epsilon^{rec}(x_0)) = c\Psi(u_0\cdot\check{x};\kappa\mu_0,k_\star)+O(\epsilon^{1/2}),\ \epsilon\to 0,\\
&c := -\frac{\kappa\omega(\alpha_\star,x_0)W(\alpha_\star,p_\star;y_0)}{\pi}(2/M)^{1/2}\,\Delta f(y_0),\\
&k_\star := \alpha_\star/\Delta\alpha,\ \kappa := \Delta\alpha/\epsilon,
\end{aligned} \tag{2.13}$$

Downloaded 09/12/24 to 5.198.137.25 . Redistribution subject to SIAM license or copyright; see https://epubs.siam.org/terms-privacy

Copyright © by SIAM. Unauthorized reproduction of this article is prohibited.

where M is defined in (2.3), u_0 and μ_0 are defined (2.6), and the $O(\epsilon^{1/2})$ term is uniform with respect to $\check{x}$ confined to any bounded set.

To help the reader, we discuss various quantities occurring in (2.13).

1. $\check{x}$ is a rescaled displacement from a fixed point x_0 to a nearby reconstruction point x: $\check{x} = (x - x_0)/\epsilon$.
2. For the classical Radon transform (CRT), $\mathcal{P}_*(\alpha, x) = \vec{\alpha} \cdot x$, where α and $\vec{\alpha}$ are related by $\vec{\alpha} = (\cos\alpha, \sin\alpha)$.
3. $\alpha_\star, p_\star$ are the values such that the integration curve $\mathcal{S}_\star = \mathcal{S}_{\alpha_\star, p_\star}$ contains x_0 and is tangent to $\mathcal{S}$ at some point, denoted y_0 (see Figure 1).
4. $W(\alpha, p; y)$ and $\omega(\alpha, x)$ are integration weights in $\mathcal{R}$ and its adjoint (see (2.1), (2.9), (2.10) and the discussion around the latter equation). For the CRT, $W(\alpha, p; y) \equiv 1$ and $\omega(\alpha, x) \equiv 1$.
5. $\kappa = \Delta\alpha/\epsilon$, where $\Delta\alpha$ is the step size along α.
6. Up to a nonzero factor, M is the difference of curvatures of $\mathcal{S}$ and $\mathcal{S}_\star$ at y_0.
7. $\Delta f(y_0)$ is the value of the jump of f across $\mathcal{S}$ at y_0.
8. $k_\star = \alpha_\star/\Delta\alpha$ is the "index" value corresponding to the angle $\alpha_\star$. We put the word index in quotes, because $k_\star$ is not necessarily an integer. As is easily seen from (2.11) and (2.13), only the fractional part of $k_\star$ is important.
9. The quantities $u_0 := \mathrm{d}_x \mathcal{P}_*(\alpha_\star, x_0)$ and $\mu_0 := \partial_\alpha(\mathcal{P}_*(\alpha_\star, x_0) - \mathcal{P}(\alpha_\star))$ depend on the properties of the Radon transform (via the function $\mathcal{P}_*$) and the curve $\mathcal{S}$. For the CRT, $u_0 = \vec{\alpha}_\star$ and $\mu_0 = \vec{\alpha}_\star^{\perp} \cdot (x_0 - y_0)$, so $|\mu_0| = |x_0 - y_0|$.

The following corollary, which follows immediately from Theorem 2.5, illustrates what (2.13) looks like in the case of the CRT.

Corollary 2.6. *Let $\mathcal{R}$ be the CRT. Under the assumptions of Theorem 2.5 one has*

$$\begin{aligned} &\epsilon^{-1/2}(f_\epsilon^{rec}(x_0 + \epsilon\check{x}) - f_\epsilon^{rec}(x_0)) = c\Psi(\vec{\alpha}_\star \cdot \check{x}; \kappa\vec{\alpha}_\star^{\perp} \cdot (x_0 - y_0), k_\star) + O(\epsilon^{1/2}),\ \epsilon \to 0, \\ &c := -(\kappa/\pi)(2r)^{1/2}\,\Delta f(y_0),\ k_\star := \alpha_\star/\Delta\alpha,\ \kappa := \Delta\alpha/\epsilon, \end{aligned} \tag{2.14}$$

where r is the radius of curvature of $\mathcal{S}$ at y_0 and the $O(\epsilon^{1/2})$ term is uniform with respect to $\check{x}$ confined to any bounded set.

See section 5 for more details on how to apply (2.13) for the classical and circular Radon transforms.

3. Proof of Theorem 2.5.

By (2.6), $u_0 \neq 0$, $\mu_0 \neq 0$. By linearity of the Radon transform, we can assume that the support of f is contained in a small neighborhood of y_0 (i.e., by shrinking U as much as necessary). By Assumption 2.1(5), shrinking U and Ω even more, we can assume that there exists $c > 0$ such that

$$\mathcal{S}_{\alpha,p} \cap U = \varnothing \text{ for any } \alpha \in \Omega, |p - p_\star| \geq c. \tag{3.1}$$

Then

$$\hat{f}(\alpha, p) = \varphi_1(\alpha)(p - \mathcal{P}(\alpha))_+^{1/2} + \varphi_2(\alpha, p)(p - \mathcal{P}(\alpha))_+^{3/2} + \varphi_3(\alpha, p),\ \alpha \in \Omega, p \in \mathbb{R}, \tag{3.2}$$

Downloaded 09/12/24 to 5.198.137.25 . Redistribution subject to SIAM license or copyright; see https://epubs.siam.org/terms-privacy

Copyright © by SIAM. Unauthorized reproduction of this article is prohibited.

where $\varphi_1 \in C_0^\infty(\Omega)$, $\varphi_{2,3} \in C^\infty(\Omega \times \mathbb{R})$, and

$$\varphi_1(\alpha_\star) = W(\alpha_\star, p_\star; y_0)\Delta f(y_0) 2(2/M)^{1/2}. \tag{3.3}$$

For the CRT this result is established in [31, 32]. For the generalized Radon transform it easily follows from $\mathrm{d}_x \mathcal{P}_*(\alpha_\star, y_0) \neq 0$ and $M \neq 0$ (see Assumptions 2.1(1) and 2.1(4)) by applying the method of proof of Lemma 3.5 in [21].

Since $f(x)$ is compactly supported, $\hat{f}(\alpha, p)$ is compactly supported in p by (3.1). Hence we can assume that $\varphi_2(\alpha, p)$ is compactly supported as well and

$$\varphi_3(\alpha, p) \equiv -\varphi_1(\alpha)(p - \mathcal{P}(\alpha))_+^{1/2}, \ \alpha \in \Omega, |p| \geq c, \tag{3.4}$$

for some c.

The idea of the proof is to split $\hat{f}$ into three terms using (3.2), substitute each of them one by one into (2.8), (2.9), and investigate the resulting expressions separately.

3.1. Beginning of proof. Estimate of the leading term. Replace $\hat{f}(\alpha, s)$ with $\varphi_1(\alpha)(s - \mathcal{P}(\alpha))_+^{1/2}$ in (2.8) and substitute into (2.9). After simple transformations we get

$$\begin{aligned} f_\epsilon^{\text{rec-1}}(x) &:= -\frac{\Delta\alpha}{2\pi\epsilon^{1/2}} \sum_{\alpha_k \in \Omega} \omega(\alpha_k, x)\varphi_1(\alpha_k)\psi((\mathcal{P}_*(\alpha_k, x) - \mathcal{P}(\alpha_k))/\epsilon), \\ \psi(\hat{q}) &:= (2\pi)^{-1} \int (\hat{p} - \hat{q})^{-1} \int w(\hat{p} - \hat{s})\hat{s}_+^{-1/2} \mathrm{d}\hat{s}\mathrm{d}\hat{p}. \end{aligned} \tag{3.5}$$

After additional transformations with the help of the integral (3.13), ψ simplifies to the expression in (2.11). These transformations are justified by applying ψ in (3.5) to a test function and changing the order of integration using the result in [33, section III.28.4]. In turn, (2.11) gives

$$\begin{aligned} &\psi(\hat{q}) = 0, \ \hat{q} > c, \quad \psi(\hat{q}) \ \text{ is uniformly continuous on } \mathbb{R}, \\ &\psi^{(n)}(\hat{q}) = c_n(-\hat{q})^{-(1/2)-n} + O(|\hat{q}|^{-(3/2)-n}), \ \hat{q} < -c, \hat{q} \to -\infty, n = 0, 1, 2, \ldots, \end{aligned} \tag{3.6}$$

for some $c > 0$ and c_n. Since $\hat{p}_+^{-1/2} \in L_{loc}^{q'}(\mathbb{R})$ for any $q' < 2$, Assumption 2.4(1) and [34, Exercise 11, p. 196] imply that ψ is uniformly continuous on $\mathbb{R}$. Note that $\psi(\hat{q})$ is of limited smoothness on a compact set, outside of which ψ is C^∞.

Using the notation in (2.6) and (2.11) we formulate the following result.

Lemma 3.1. *Under the assumptions of Theorem 2.5 one has*

$$\begin{aligned} &\epsilon^{-1/2}(f_\epsilon^{\text{rec-1}}(x_0 + \epsilon\check{x}) - f_\epsilon^{\text{rec-1}}(x_0)) \\ &\quad = -\frac{\kappa\omega(\alpha_\star, x_0)\varphi_1(\alpha_\star)}{2\pi} \Psi(u_0 \cdot \check{x}; \mu_0\kappa, k_\star) + O(\epsilon^{1/2}), \end{aligned} \tag{3.7}$$

where the $O(\epsilon^{1/2})$ term is uniform with respect to $\check{x}$ confined to any bounded set.

The proof of the lemma is in subsection A.2.

Downloaded 09/12/24 to 5.198.137.25 . Redistribution subject to SIAM license or copyright; see https://epubs.siam.org/terms-privacy

Copyright © by SIAM. Unauthorized reproduction of this article is prohibited.

3.2. The second term. Similarly, replace $\hat{f}(\alpha,s)$ with $\varphi_2(\alpha,s)(s-\mathcal{P}(\alpha))_+^{3/2}$ in (2.8) and substitute into (2.9). After simple transformations we get with some c

$$
\begin{aligned}
f_\epsilon^{\text{rec-2}}(x) &:= c\epsilon \sum_{\alpha_k\in\Omega} \omega(\alpha_k,x) g_2(\mathcal{P}_*(\alpha_k,x),\mathcal{P}(\alpha_k),\alpha_k),\ \ x = x_0+\epsilon\check{x},\\
g_2(p,q,\alpha) &:= \int (t-p)^{-1}\partial_t \int w_\epsilon(t-s)\varphi_2(\alpha,s)(s-q)_+^{3/2}\mathrm{d}s\mathrm{d}t,\\
&\quad p=\mathcal{P}_*(\alpha_k,x),\ \ q=\mathcal{P}(\alpha_k).
\end{aligned}
\tag{3.8}
$$

Therefore, in (3.8) p,q satisfy

$$
|p| \le \sup_{\alpha\in\Omega} |\mathcal{P}_*(\alpha,x_0)| + O(\epsilon),\ \ |q|\le c,
\tag{3.9}
$$

where c is the same as in (3.1). Reducing, if necessary, Ω further, we can assume that the supremum in (3.9) is bounded. Thus, $|p|,|q| \le P$ for some $P<\infty$. For simplicity, the dependence of g_2, φ_2, and related functions on α will be omitted from notation. Rewrite g_2 as follows:

$$
g_2(p,q) = \int w_\epsilon(p-t)\int (s-t)^{-1}\partial_s\left(\varphi_2(s)(s-q)_+^{3/2}\right)\mathrm{d}s\mathrm{d}t.
\tag{3.10}
$$

Using the results in [35, section 8.3], we find

$$
g_2(p,q) = \int w_\epsilon(p-t)\left(\varphi_{2,1}(t,q)(t-q)_-^{1/2} + \varphi_{2,2}(t,q)\right)\mathrm{d}t
\tag{3.11}
$$

for some smooth and bounded $\varphi_{2,1}$ and $\varphi_{2,2}$. The same result can be obtained by elementary means by writing

$$
\int_0^\infty \frac{\varphi(s)}{s^{1/2}(s-\rho)}\mathrm{d}s = \varphi(\rho)\int_0^\infty \frac{\mathrm{d}s}{s^{1/2}(s-\rho)} + \int_0^\infty \frac{\varphi(s)-\varphi(\rho)}{s-\rho}s^{-1/2}\mathrm{d}s,
\tag{3.12}
$$

using the integral (see [36, equations 2.2.4.25 and 2.2.4.26])

$$
\int (s-\rho)^{-1}s_+^{-1/2}\mathrm{d}s = \pi\rho_-^{-1/2},
\tag{3.13}
$$

and substituting $\rho = t-q$, $\varphi(s) = s[(3/2)\varphi_2(s+q)+s\varphi_2'(s+q)]$.

From (3.11) it follows that

$$
\begin{aligned}
&|g_2(p+\Delta p,q)-g_2(p,q)|\\
&\le O(|\Delta p|) + c\max_{|\tau|\le c\epsilon}\left|(p-q+\Delta p+\tau)_-^{1/2} - (p-q+\tau)_-^{1/2}\right|
\end{aligned}
\tag{3.14}
$$

for some c. Recall that in (3.14)

$$
p-q = \mathcal{P}_*(\alpha_k,x_0)-\mathcal{P}(\alpha_k),\ \ \Delta p = \mathcal{P}_*(\alpha_k,x)-\mathcal{P}_*(\alpha_k,x_0) = O(\epsilon),\ \ \tau = O(\epsilon),
\tag{3.15}
$$

where $x = x_0+\epsilon\check{x}$. Since $\mu_0\neq 0$ (cf. (2.6)), we have $|\mathcal{P}_*(\alpha,x_0)-\mathcal{P}(\alpha)| \ge c|\alpha-\alpha_\star|$ for any $\alpha\in\Omega$ and some $c>0$. Therefore, there exists $c_1>0$ such that whenever $|\alpha-\alpha_\star|\ge c_1\epsilon$ and

Downloaded 09/12/24 to 5.198.137.25 . Redistribution subject to SIAM license or copyright; see https://epubs.siam.org/terms-privacy

Copyright © by SIAM. Unauthorized reproduction of this article is prohibited.

$\epsilon > 0$ is sufficiently small, the expressions $(p-q+\Delta p+\tau)_-^{1/2}$ and $(p-q+\tau)_-^{1/2}$ are either both zero or both nonzero. When they are both nonzero, the magnitude of their difference equals

$$\frac{|\Delta p|}{|p-q+\Delta p+\tau|^{1/2}+|p-q+\tau|^{1/2}} \leq \frac{c\epsilon}{|\alpha-\alpha_\star|^{1/2}}, \quad |\alpha-\alpha_\star| \geq c_1\epsilon, \tag{3.16}$$

for some c. Also, there are finitely many k (close to $k_\star$) such that $|\alpha_k - \alpha_\star| < c_1\epsilon$. For those k, the same difference is $O(\epsilon^{1/2})$.

Using (3.14) and (3.16) in (3.8), we find, similarly to (2.13),

$$\begin{aligned} &\epsilon^{-1/2}(f_\epsilon^{\text{rec-2}}(x_0+\epsilon\check{x}) - f_\epsilon^{\text{rec-2}}(x_0)) \\ &\quad = O(\epsilon^{1/2}) + O(\epsilon^{1/2})\left[\epsilon^{1/2} + \sum_{1\leq k\leq O(1/\epsilon)} \frac{\epsilon}{(k\epsilon)^{1/2}}\right] = O(\epsilon^{1/2}). \end{aligned} \tag{3.17}$$

The first $O(\epsilon^{1/2})$ term on the right in (3.17) absorbs the contributions, which arise due to the x-dependence of ω in (3.8) and due to the $O(|\Delta p|) = O(\epsilon)$ term in (3.14). Here we use that $|\omega(x_0+\epsilon\check{x},\alpha)-\omega(x_0,\alpha)| \leq c\epsilon$ and $|g_2(p,q,\alpha)| \leq c$ for some c and all $\alpha \in \Omega$, $|p|, |q| \leq P$.

3.3. The third term. Finally, replace $\hat{f}(\alpha,s)$ with $\varphi_3(\alpha,s)$ in (2.8) and substitute this into (2.9). Recall that φ_3 is not necessarily compactly supported in s (cf. (3.4)) and

$$\partial_s^l \varphi_3(\alpha,s) = O(|s|^{(1/2)-l}), \ s\to\infty, \ \alpha\in\Omega, \ l=0,1,2, \tag{3.18}$$

where the big-O term is uniform in α. Similarly to (3.8) and (3.10), we find

$$\begin{aligned} f_\epsilon^{\text{rec-3}}(x) &:= c\epsilon \sum_{\alpha_k\in\Omega} \omega(\alpha_k,x) g_3(\mathcal{P}_*(\alpha_k,x),\alpha_k), \\ g_3(p,\alpha) &:= \int (t-p)^{-1}\partial_t \int w_\epsilon(t-s)\varphi_3(\alpha,s)\mathrm{d}s\mathrm{d}t \\ &= \int w_\epsilon(-\tau)\int s^{-1}\partial_s\varphi_3(\alpha,s+\tau+p)\mathrm{d}s\mathrm{d}\tau, \ |p|\leq P. \end{aligned} \tag{3.19}$$

The following lemma is proven in Appendix A.3.

Lemma 3.2. *One has*

$$\int s^{-1}\partial_s\left[\varphi_3(\alpha,s+q+\Delta q)-\varphi_3(\alpha,s+q)\right]ds = O(|\Delta q|), \ \Delta q\to 0, \tag{3.20}$$

uniformly in $\alpha\in\Omega$, $|q|\leq c$, *for any* c.

Using Lemma 3.2, the analogue of (3.14) becomes (with Δp the same as in (3.15))

$$\begin{aligned} &|g_3(p+\Delta p,\alpha) - g_3(p,\alpha)| \\ &\quad \leq c\max_{|\tau|\leq c\epsilon}\left|\int s^{-1}\partial_s\left[\varphi_3(\alpha,s+\tau+p+\Delta p)-\varphi_3(\alpha,s+\tau+p)\right]\mathrm{d}s\right| \\ &\quad = O(|\Delta p|) = O(\epsilon), \ \alpha\in\Omega, \end{aligned} \tag{3.21}$$

for some c. Hence, we obtain, similarly to (3.17),

$$\epsilon^{-1/2}(f_\epsilon^{\text{rec-3}}(x_0+\epsilon\check{x}) - f_\epsilon^{\text{rec-3}}(x_0)) = O(\epsilon^{1/2}). \tag{3.22}$$

Combining (2.13), (3.3), (3.17), (3.22), and using that $f_\epsilon^{\text{rec}} = f_\epsilon^{\text{rec-1}} + f_\epsilon^{\text{rec-2}} + f_\epsilon^{\text{rec-3}}$, we finish the proof of Theorem 2.5.

Copyright © by SIAM. Unauthorized reproduction of this article is prohibited.

Downloaded 09/12/24 to 5.198.137.25 . Redistribution subject to SIAM license or copyright; see https://epubs.siam.org/terms-privacy

Downloaded 09/12/24 to 5.198.137.25 . Redistribution subject to SIAM license or copyright; see https://epubs.siam.org/terms-privacy

4. A more detailed look at the function Ψ.

4.1. Properties of the function Ψ.

Theorem 2.5 shows that the function Ψ defined in (2.11) plays a key role in the description of the aliasing artifact. By (3.6), the series that defines Ψ converges absolutely at every point. Here we prove some properties of Ψ.

Lemma 4.1. *Under Assumption 2.4 one has*

1. Ψ *is continuous on* $\mathbb{R}\times(\mathbb{R}\setminus 0)\times\mathbb{R}$;
2. $\Psi(h;a,r+1)=\Psi(h;a,r)$ *and* $\Psi(h;-a,-r)=\Psi(h;a,r)$ *for all* $h,a,r\in\mathbb{R}$;
3. $\Psi(h+a;a,r)=\Psi(h;a,r)$ *for all* $h,a,r\in\mathbb{R}$.

Remark 4.2. In this section, Ψ is viewed as a stand-alone function (i.e., unrelated to its use in Theorem 2.5). Therefore, its arguments h, a, and r temporarily lose the meaning they have when $\Psi(h;a,r)$ is used in Theorem 2.5. Nevertheless, when reading this section it may be helpful to remember that in the setting of the CRT, $h=\vec{\alpha}_\star\cdot\check{x}$, $a=\kappa\vec{\alpha}_\star^{\perp}\cdot(x_0-y_0)$, and $r=k_\star$ (see Corollary 2.6).

Proof. When a is bounded away from zero, the number of terms with limited smoothness in the sum in (2.11) is uniformly bounded when h and r are confined to a bounded set. Hence we can represent Ψ as a sum of finitely many continuous terms and an absolutely convergent series, whose terms are smooth functions. This proves statement (1).

The first half of statement (2) is obvious. The second half of statement (2) follows immediately by replacing $a\to -a$, $r\to -r$ in (2.11), and changing the index of summation $k\to -k$.

To prove statement (3), fix some $c\gg 1$ and shift the index of summation $k'=k+1$ in (2.11):

$$\Psi(h+a;a,r)=\sum_{k'\le c}\left[\psi\left(a(k'-r)+h\right)-\psi\left(a(k'-1-r)\right)\right]. \tag{4.1}$$

At first glance, to finish the proof we can just change back $k=k'-1$ in the second ψ. This does not work, since each of the sums taken separately is divergent (cf. (3.6)). Hence we argue differently. We have for any $K\gg 1$,

$$\begin{aligned}\Psi(h+a;a,r)&=\sum_{k'=-K}^{c}\left[\psi(a(k'-r)+h)-\psi(a(k'-1-r))\right]+O(K^{-1/2})\\&=\sum_{k'=-K}^{c}\left[\psi(a(k'-r)+h)-\psi(a(k'-r))\right]-\psi(a(K-1-r))\\&\quad+O(K^{-1/2})=\Psi(h;a,r)+O(K^{-1/2}),\ K\to\infty.\end{aligned} \tag{4.2}$$

The desired assertion now follows. ∎

Lemma 4.3. *Suppose* w *is compactly supported and* $w^{(N)}\in L^q(\mathbb{R})$ *for some* $N\ge 1$ *and* $q>2$. *One has*

$$\partial_h^{n_1}\partial_r^{n_2}\Psi(h;a,r)=O(|a|^{N-(n_1+n_2)}),\ a\to 0,\ n_1,n_2\ge 0, n_1+n_2\le N-1, \tag{4.3}$$

uniformly in $h,r\in\mathbb{R}$.

Copyright © by SIAM. Unauthorized reproduction of this article is prohibited.

Proof. We need the following simple lemma, which follows immediately from the Euler–MacLaurin summation formula [37, equation (25.7)]. For convenience of the reader, the lemma is proven in Appendix A.4.

Lemma 4.4. *Pick some $N' \geq 1$. Suppose $g, g^{(N')} \in L^1(\mathbb{R})$, $g^{(n)}(t) \to 0$ as $t \to \infty$ for any $n = 0, 1, 2, \ldots, N' - 1$, and $\int_{\mathbb{R}} g(x)dx = 0$. Then,*

$$\left| \epsilon \sum_{k \in \mathbb{Z}} g(\epsilon k) \right| \leq c \epsilon^{N'} \| g^{(N')} \|_{L^1(\mathbb{R})} \tag{4.4}$$

for some c independent of g and ϵ.

Set

$$g(t) := \partial_h^{n_1} \partial_r^{n_2} (\psi(t - ar + h) - \psi(t - ar)). \tag{4.5}$$

The dependence of g on h and r is omitted for simplicity. As is easily seen, g satisfies the assumptions of Lemma 4.4. Indeed, due to Lemma 4.1(2), 4.1(3), we can assume $h \in [0, a)$, $r \in [0, 1)$. The assumption $w^{(N)} \in L^q(\mathbb{R})$, $q > 2$ and (2.11) imply that all the derivatives of ψ up to the order N are continuous on $\mathbb{R}$.

From (3.6), $|g^{(m)}(t)| \leq c_m (1 + |t|)^{-3/2}$, $0 \leq m \leq N - (n_1 + n_2)$, for some c_m independent of h and r. Hence g decays sufficiently fast at infinity.

It remains to check that g integrates to zero. If $n_1 > 0$ or $n_2 > 0$, this is obvious. Suppose $n_1 = n_2 = 0$. For some $c > 0$,

$$\begin{aligned} \int_{\mathbb{R}} g(t) \mathrm{d}t &= \int_{-A}^{c} g(t) \mathrm{d}t + O(A^{-1/2}) \\ &= -\int_{-A}^{h-A} \psi(t) \mathrm{d}t + O(A^{-1/2}) = O(A^{-1/2}), \ A \to \infty. \end{aligned} \tag{4.6}$$

Application of Lemma 4.4 to g in (4.5) with $\epsilon = a$ and $N_1 = N - (n_1 + n_2)$ proves the desired assertion. The uniformity with respect to h and r is obvious.

Corollary 4.5. *Suppose w is compactly supported and $w^{(N)} \in L^q(\mathbb{R})$ for some $N \geq 1$ and $q > 2$. Then the derivatives $\partial_h^{n_1} \partial_r^{n_2} \Psi(h; a, r)$, $n_1, n_2 \geq 0$, $n_1 + n_2 \leq N - 1$, are continuous for all values of their arguments.*

Proof. The continuity away from $a = 0$ is proven the same way as assertion (1) of Lemma 4.1. The continuity at $a = 0$ follows from Lemma 4.3. ∎

4.2. Computing Ψ numerically. Numerically, we compute Ψ using the following approach. Due to Lemma 4.1(2) and 4.1(3), we assume $h \in [0, a)$, $r \in [0, 1)$. The mollifier in our experiments is given by

$$w(t) = (15/16)(1 - t^2)_+^2. \tag{4.7}$$

First, $\psi(t)$ is computed by analytically evaluating the integral in (2.11). Then we compute $\Delta\psi(t, h) := \psi(t + h) - \psi(t)$. For moderate values of t we compute $\Delta\psi$ directly from the definition. For $t \ll -1$ we use

$$\Delta\psi(t, h) \approx h/(4|t|^{3/2}). \tag{4.8}$$

Copyright © by SIAM. Unauthorized reproduction of this article is prohibited.

Downloaded 09/12/24 to 5.198.137.25 . Redistribution subject to SIAM license or copyright; see https://epubs.siam.org/terms-privacy

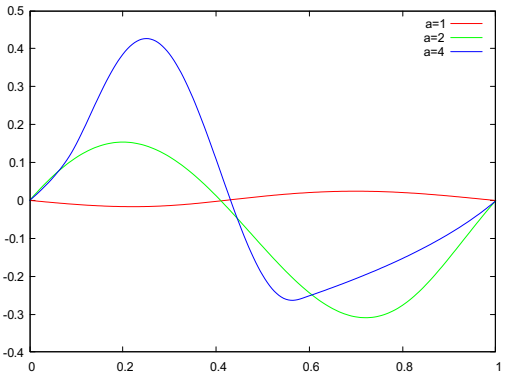

Figure 3. *Plots of $\Psi(ah';a,r)$ for three values of a. The variable h' is on the horizontal axis.*

Finally, we write

$$\Psi(h;a,r) \approx \sum_{k=-K+1}^{c} \Delta\psi(a(k-r),h) + \frac{h}{4|a|^{3/2}} \sum_{k=K}^{\infty} k^{-3/2}, \tag{4.9}$$

where $c > 0$ is selected so that $\Delta\psi(a(k-r),h) = 0$ for all $k > c$ and $h \in [0,a)$ and $K \gg 1$. The last sum is estimated using the asymptotic formula for the Hurwitz zeta function [38, equation (1.1)]

$$\zeta(s,t) := \sum_{k=0}^{\infty} (k+t)^{-s} = \frac{t^{1-s}}{s-1} + \frac{t^{-s}}{2} + O(t^{-(s+1)}),\ t \to +\infty, \tag{4.10}$$

where $s = 3/2$ and $t = K$. The plots of $\Psi(ah';a,r)$, $0 \le h' \le 1$, for the values $a = 1,2,4$ and $r = 1/3$ are shown in Figure 3.

In agreement with Lemma 4.3, we see that $\Psi(ah';a,r)$ decays rapidly as $a \to 0$.

5. Numerical experiments.

5.1. CRT.

In this subsection we experiment with the CRT, which integrates over lines:

$$\hat{f}(\alpha,p) = \int_{S_{\alpha,p}} f(x)\mathrm{d}x,\ \vec{\alpha} = (\cos\alpha, \sin\alpha),\ S_{\alpha,p} := \{x \in \mathbb{R}^2 : \alpha \cdot x = p\}. \tag{5.1}$$

Reconstruction uses (2.9),

$$\begin{aligned} f_\epsilon^{\mathrm{rec}}(x) &= -\frac{\Delta\alpha}{2\pi} \sum_{|\alpha_k| \le \pi/2} \frac{1}{\pi} \int \frac{\partial_p \hat{f}_\epsilon(\alpha_k,p)}{p - \mathcal{P}_*(x,\alpha_k)} \mathrm{d}p,\ \mathcal{P}_*(x,\alpha) \equiv \vec{\alpha} \cdot x, \\ \hat{f}_\epsilon(\alpha_k,p) &= \int w_\epsilon(p-\rho)\hat{f}(\alpha_k,\rho)\mathrm{d}\rho,\ \alpha_k = -(\pi/2) + (\pi/N_\alpha)(k+\delta), \end{aligned} \tag{5.2}$$

and w is the same as in (4.7). The weights in both the Radon transform and the inversion formula are set to 1: $W(\alpha,p;x) \equiv 1$, $\omega(\alpha,x) \equiv 1$.

Copyright © by SIAM. Unauthorized reproduction of this article is prohibited.

Downloaded 09/12/24 to 5.198.137.25 . Redistribution subject to SIAM license or copyright; see https://epubs.siam.org/terms-privacy

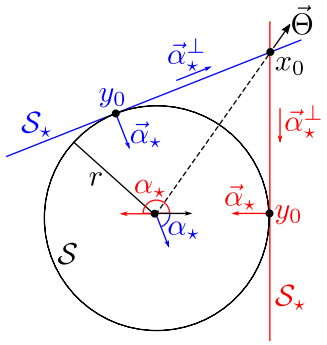

Figure 4. *Illustration of various quantities used in the main formula (2.13) to predict aliasing from a disk in the case of the CRT.*

In the first experiment, f is the characteristic function of the disk centered at the origin with radius r. Thus, $\mathcal{S} = \{x \in \mathbb{R}^2 : |x| = r\}$. By (2.2),

$$|\mathrm{d}H(y_0)| = |\mathrm{d}_x \mathcal{P}_*(\alpha_\star, y_0)| = |\alpha_\star| = 1. \tag{5.3}$$

Therefore, by (2.3),

$$M = -(\vec{\Theta}_0^\perp \cdot \partial_y)^2 H(y)|_{y=y_0} = 1/r > 0 \tag{5.4}$$

is the curvature of $\mathcal{S}$ at y_0. Also, $\vec{\Theta}_0 = \mathrm{d}H(y_0)$ points towards the center of curvature of $\mathcal{S}$ at y_0 (the center of the disk).

At a given $x \notin \mathcal{S}$, aliasing arises due to the parts of $\mathcal{S}$ where the lines $\mathcal{S}_{\alpha,p} \ni x$ are tangent to $\mathcal{S}$. For $|x| > r$, two such lines exist. We pick $x_0 = (r, b)$ and find two pairs $(\alpha_\star, p_\star)$ with the required properties. Clearly, one of the pairs is $(\alpha_\star = \pi, p_\star = -r)$, and the other is $(\alpha_\star = 2\tan^{-1}(b/r) - \pi, p_\star = -r)$. This choice of values of $(\alpha_\star, p_\star)$ ensures that $\mathcal{S}_{\alpha_\star, p_\star + \delta}$, where $0 < \delta \ll 1$, intersects $\mathcal{S}$ at two points (cf., the paragraph following (2.3)). See Figure 4, where the first pair (with $\alpha_\star = \pi$) is shown in red, and the second, in black. The contribution coming from a neighborhood of each point of tangency y_0 is computed by (2.13) using the corresponding values of parameters (computed elsewhere in this subsection) and added. For reconstructions we use $r = 5$ and $x_0 = (5, 7)$. To better illustrate the aliasing artifact we also reconstruct a small region of interest (ROI), which is a square centered at x_0 with side length 40ϵ.

For computations we also need u_0 and μ_0 (cf. (2.13)). They follow easily from (2.6),

$$u_0 = \vec{\alpha}_\star, \ \ \mu_0 = \vec{\alpha}_\star^\perp \cdot (x_0 - y_0), \tag{5.5}$$

where y_0 is the point where $\mathcal{S}_\star$ is tangent to $\mathcal{S}$. As is seen from Figure 4, $\mu_0 = -|x_0 - y_0|$ for the first (red) pair $(\alpha_\star, p_\star)$, and $\mu_0 = |x_0 - y_0|$ for the second (black) pair.

In the first experiment, $\epsilon = 0.02$, $N_\alpha = 200$ and in the second, $\epsilon = 0.01$, $N_\alpha = 400$. Since the direction $\alpha_\star = 0$ is special, we use a nonzero shift δ in (5.2) for additional generality. The results are shown in Figures 5–10.

Figure 5 (left panel) shows the reconstructed region $|x_1|, |x_2| \le 10$ with $\epsilon = 0.02$ and $N_\alpha = 200$. The left panel also shows the ROI (a small square). The right panel shows a

Downloaded 09/12/24 to 5.198.137.25 . Redistribution subject to SIAM license or copyright; see https://epubs.siam.org/terms-privacy

Copyright © by SIAM. Unauthorized reproduction of this article is prohibited.

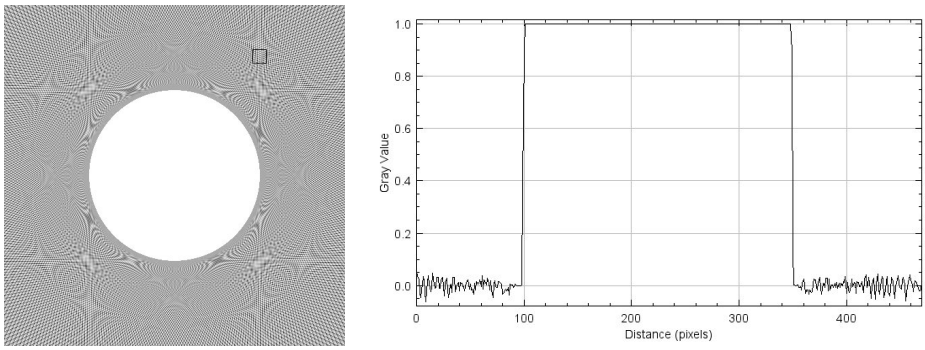

Figure 5. *Disk phantom, CRT reconstruction of the region* $|x_1|, |x_2| \le 10$*:* $\epsilon = 0.02$*,* $N_\alpha = 200$*,* $\delta = 0.03$*. Left: global reconstruction; right: profile of the reconstruction through the center.*

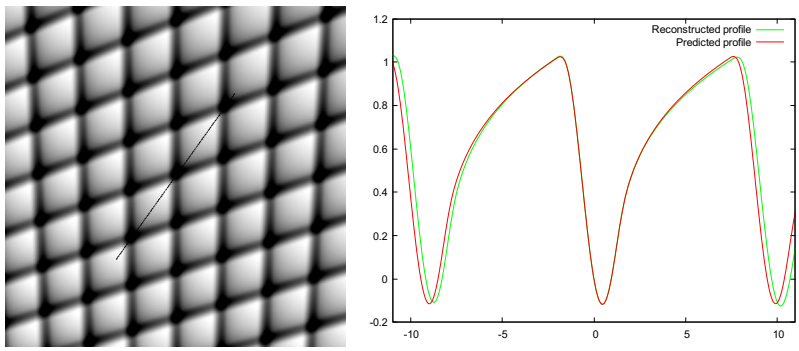

Figure 6. *Disk phantom, ROI CRT reconstruction:* $\epsilon = 0.02$*,* $N_\alpha = 200$*,* $\delta = 0.03$*. The ROI is the square shown in Figure 5. Left: reconstructed ROI; right: reconstructed (green) and predicted (red) profiles along the line segment* $x = x_0 + \epsilon h\vec{\Theta}$*,* $|h| \le 11$*, shown on the left. The variable* h *is on the horizontal axis.*

line profile through the origin to confirm the accuracy of reconstruction. Figure 6 shows the reconstructed ROI with $\delta = 0.03$. The right panel shows the profiles of the reconstructed difference $\epsilon^{-1/2}(f_\epsilon^{\mathrm{rec}}(x) - f_\epsilon^{\mathrm{rec}}(x_0))$ (green) and the prediction given by the main term on the right in (2.13) (red) along the line segment $x = x_0 + \epsilon h\vec{\Theta}$, $|h| \le 11$, where $\vec{\Theta} = x_0/|x_0|$. The line segment is indicated on the left panel. The values of h are on the horizontal axis of the profile. From (5.5), the values of $u_0 \cdot \check{x}$ used in (2.13) are given by $h\,\vec{\alpha}_\star \cdot \Theta$.

Similarly, Figure 7 shows the reconstructed ROI and line profiles for the same line segment when $\delta = 0.2$.

Figure 8 shows the reconstructed region $|x_1|, |x_2| \le 10$ with $\epsilon = 0.01$ and $N_\alpha = 400$. The ROI is shown as well. Recall that the size of the ROI is proportional to ϵ. Figure 9 shows the ROI and the corresponding line profiles for $\delta = 0.03$. Similarly, Figure 10 shows the reconstructed ROI and line profiles when $\delta = 0.2$. In both cases, the vector $\vec{\Theta}$ and the range of h that determine the line segment are the same as before.

Comparing Figure 6 with Figure 9 and Figure 7 with Figure 10, we see that reducing ϵ and $\Delta\alpha$ improves the match between the reconstruction and prediction.

Copyright © by SIAM. Unauthorized reproduction of this article is prohibited.

Downloaded 09/12/24 to 5.198.137.25 . Redistribution subject to SIAM license or copyright; see https://epubs.siam.org/terms-privacy

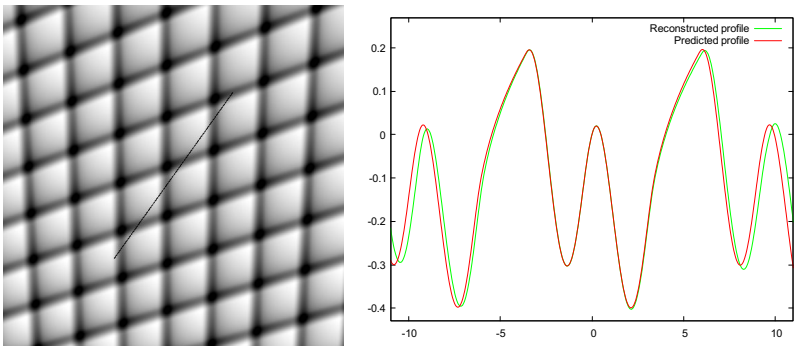

Figure 7. *Disk phantom, ROI CRT reconstruction:* $\epsilon = 0.02$, $N_\alpha = 200$, $\delta = 0.2$. *The ROI is the square shown on the left in Figure 5. Left: reconstructed ROI; right: reconstructed (green) and predicted (red) profiles along the line segment* $x = x_0 + \epsilon h\vec{\Theta}$, $|h| \le 11$, *shown on the left. The variable* h *is on the horizontal axis.*

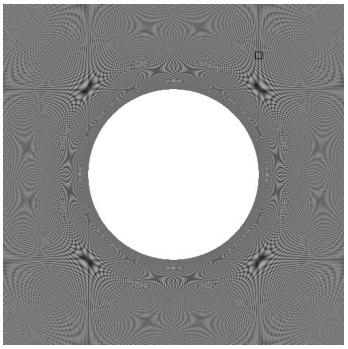

Figure 8. *Disk phantom, CRT reconstruction of the region* $|x_1|, |x_2| \le 10$*:* $\epsilon = 0.01$, $N_\alpha = 400$, $\delta = 0.03$.

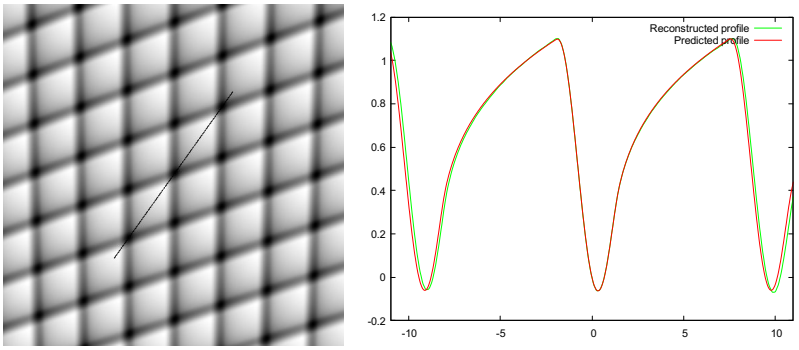

Figure 9. *Disk phantom, ROI CRT reconstruction:* $\epsilon = 0.01$, $N_\alpha = 400$, $\delta = 0.03$. *The ROI is the square shown in Figure 8. Left: reconstructed ROI; right: reconstructed (green) and predicted (red) profiles along the line segment* $x = x_0 + \epsilon h\vec{\Theta}$, $|h| \le 11$, *shown on the left. The variable* h *is on the horizontal axis.*

In the second experiment f is the characteristic function of an ellipse centered at the origin: $\mathcal{S} = \{x \in \mathbb{R}^2 : x = (r_1 \cos\theta, r_2 \sin\theta), \theta \in [0, 2\pi)\}$. Of course, the main formulas like (5.3), (5.5) still hold. The only difference is that now the radius of curvature r (and the constant M; see (5.4)) depends on the point of tangency.

Copyright © by SIAM. Unauthorized reproduction of this article is prohibited.

Downloaded 09/12/24 to 5.198.137.25 . Redistribution subject to SIAM license or copyright; see https://epubs.siam.org/terms-privacy

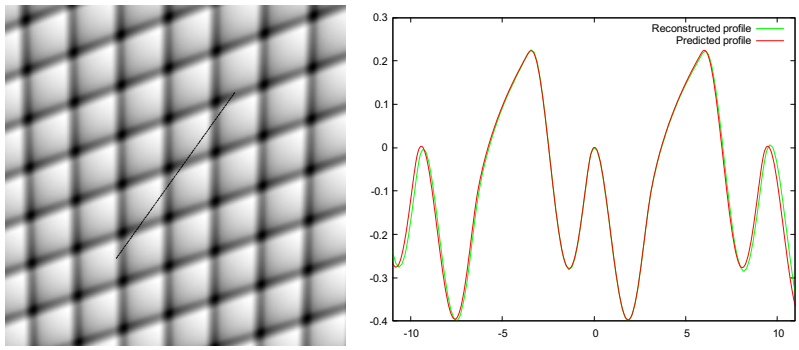

Figure 10. *Disk phantom, ROI CRT reconstruction: $\epsilon = 0.01$, $N_\alpha = 400$, $\delta = 0.2$. The ROI is the square shown in Figure 8. Left: reconstructed ROI; right: reconstructed (green) and predicted (red) profiles along the line segment $x = x_0 + \epsilon h\vec{\Theta}$, $|h| \le 11$, shown on the left. The variable h is on the horizontal axis.*

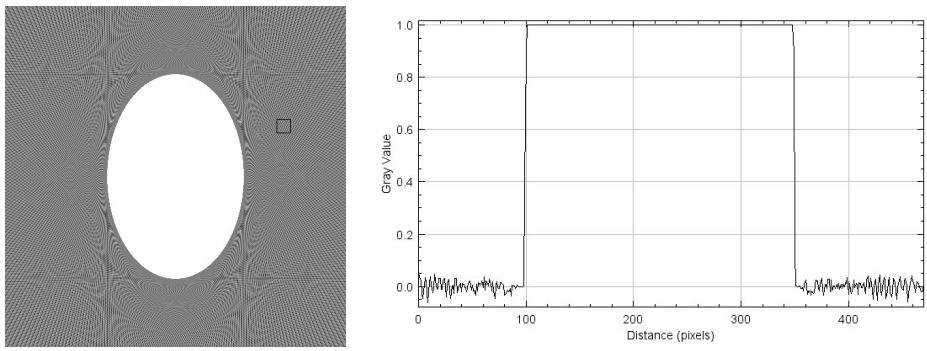

Figure 11. *Ellipse phantom, CRT reconstruction of the region $|x_1|, |x_2| \le 10$: $\epsilon = 0.02$, $N_\alpha = 200$, $\delta = 0.03$. Left: global reconstruction; right: profile of the reconstruction along the diagonal from top left to bottom right.*

As before, we pick x_0 outside the ellipse and find two pairs $(\alpha_\star, p_\star)$. The contribution coming from a neighborhood of each point of tangency y_0 is computed by (2.13) and added. In the reconstructions we use $r_1 = 4$, $r_2 = 6$, and $x_0 = 7(\cos\theta, \sin\theta)$, $\theta = 25°$. To better illustrate the aliasing artifact we also reconstruct a small ROI, which is a square centered at x_0 with side length 40ϵ.

The values of the parameters ϵ, N_α, and δ are the same as before. In the first experiment with the ellipse, $\epsilon = 0.02$, $N_\alpha = 200$ and in the second – $\epsilon = 0.01$, $N_\alpha = 400$. The results are shown in Figures 11–16.

Figure 11 (left panel) shows the reconstructed region $|x_1|, |x_2| \le 10$ with $\epsilon = 0.02$ and $N_\alpha = 200$. The left panel also shows the ROI (a small square). The right panel shows a line profile through the origin to confirm the accuracy of reconstruction. Figure 12 shows the reconstructed ROI with $\delta = 0.03$. The right panel shows the profiles of the reconstructed difference $\epsilon^{-1/2}(f_\epsilon^{\rm rec}(x) - f_\epsilon^{\rm rec}(x_0))$ (green) and the prediction given by the main term on the right in (2.13) (red) along the line segment $x = x_0 + \epsilon h\vec{\Theta}$, $|h| \le 11$, where $\vec{\Theta} = x_0/|x_0|$. The line segment is indicated on the left panel. Similarly, Figure 13 shows the reconstructed ROI and line profiles for the same line segment when $\delta = 0.2$.

Downloaded 09/12/24 to 5.198.137.25 . Redistribution subject to SIAM license or copyright; see https://epubs.siam.org/terms-privacy

Copyright © by SIAM. Unauthorized reproduction of this article is prohibited.

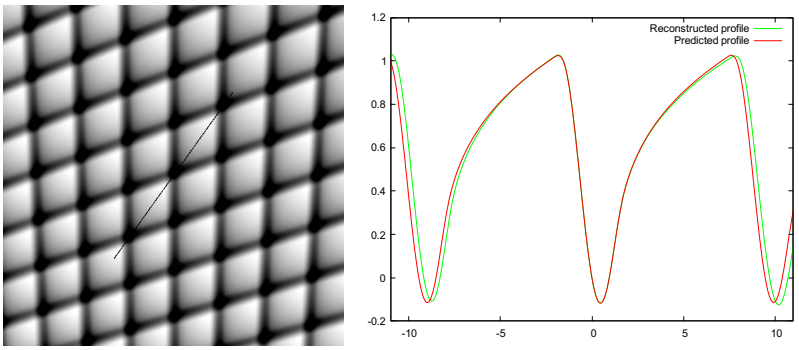

Figure 12. *Ellipse phantom, ROI CRT reconstruction: $\epsilon = 0.02$, $N_\alpha = 200$, $\delta = 0.03$. The ROI is the square shown in Figure 11. Left: reconstructed ROI; right: reconstructed (green) and predicted (red) profiles along the line segment $x = x_0 + \epsilon h\vec{\Theta}$, $|h| \le 11$, shown on the left. The variable h is on the horizontal axis.*

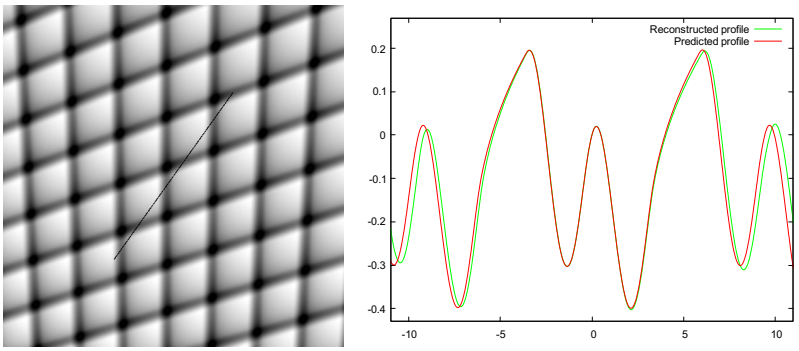

Figure 13. *Ellipse phantom, ROI CRT reconstruction: $\epsilon = 0.02$, $N_\alpha = 200$, $\delta = 0.2$. The ROI is the square shown on the left in Figure 11. Left: reconstructed ROI; right: reconstructed (green) and predicted (red) profiles along the line segment $x = x_0 + \epsilon h\vec{\Theta}$, $|h| \le 11$, shown on the left. The variable h is on the horizontal axis.*

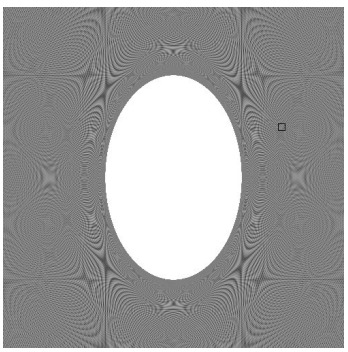

Figure 14. *Ellipse phantom, CRT reconstruction of the region $|x_1|, |x_2| \le 10$: $\epsilon = 0.01$, $N_\alpha = 400$, $\delta = 0.03$.*

Figure 14 shows the reconstructed region $|x_1|, |x_2| \le 10$ with $\epsilon = 0.01$ and $N_\alpha = 400$. The ROI is shown as well. Figure 15 shows the ROI and the corresponding line profiles for $\delta = 0.03$. Similarly, Figure 16 shows the reconstructed ROI and line profiles when $\delta = 0.2$.

Copyright © by SIAM. Unauthorized reproduction of this article is prohibited.

Downloaded 09/12/24 to 5.198.137.25 . Redistribution subject to SIAM license or copyright; see https://epubs.siam.org/terms-privacy

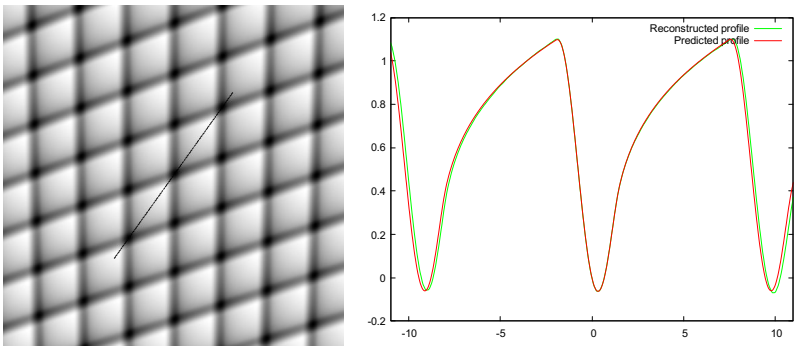

Figure 15. *Ellipse phantom, ROI CRT reconstruction:* $\epsilon = 0.01$, $N_\alpha = 400$, $\delta = 0.03$. *The ROI is the square shown in Figure* 14. *Left: reconstructed ROI; right: reconstructed (green) and predicted (red) profiles along the line segment* $x = x_0 + \epsilon h\vec{\Theta}$, $|h| \le 11$, *shown on the left. The variable* h *is on the horizontal axis.*

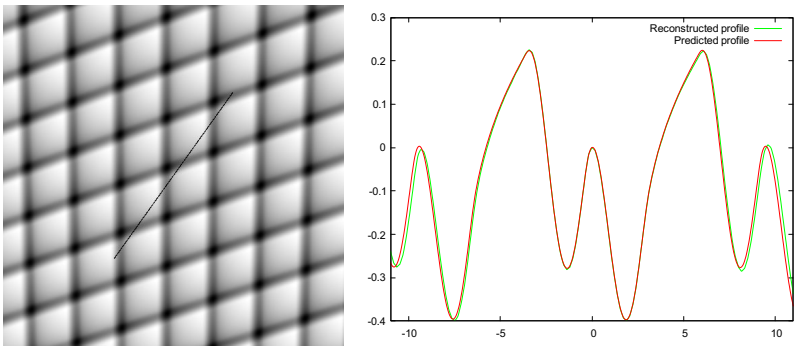

Figure 16. *Ellipse phantom, ROI CRT reconstruction:* $\epsilon = 0.01$, $N_\alpha = 400$, $\delta = 0.2$. *The ROI is the square shown in Figure* 14. *Left: reconstructed ROI; right: reconstructed (green) and predicted (red) profiles along the line segment* $x = x_0 + \epsilon h\vec{\Theta}$, $|h| \le 11$, *shown on the left. The variable* h *is on the horizontal axis.*

In both cases, the vector $\vec{\Theta}$ and the range of h that determine the line segment are the same as before.

Comparing Figure 12 with Figure 15 and Figure 13 with Figure 16, we see that reducing ϵ and $\Delta\alpha$ improves the match between the reconstruction and prediction. Overall, the results with the elliptical phantom are very similar to those with the disk phantom.

5.2. Circular Radon transform. In this subsection we experiment with the generalized Radon transform (GRT), which integrates over circles with any radius $\rho > 0$ and centers on the circle $|x| = R$:

$$(\mathcal{R}f)(\alpha,\rho) = \hat{f}(\alpha,\rho) = \int_{S_{\alpha,\rho}} f(x)\mathrm{d}x,\ \ \vec{\alpha} = (\cos\alpha, \sin\alpha), \tag{5.6}$$
$$\mathcal{P}_*(\alpha,x) := |x - R\vec{\alpha}|,\ \ S_{\alpha,\rho} := \{x \in \mathbb{R}^2 : |x - R\vec{\alpha}| = \rho\}.$$

The value of R is fixed. Therefore

$$\mathrm{d}_x\mathcal{P}_*(\alpha,x) = \frac{x - R\vec{\alpha}}{|x - R\vec{\alpha}|},\ \ M = (1/\rho_\star) - (\vec{\Theta}_0^{\perp}\cdot\partial_y)^2 H(y)|_{y=y_0} > 0. \tag{5.7}$$

Downloaded 09/12/24 to 5.198.137.25 . Redistribution subject to SIAM license or copyright; see https://epubs.siam.org/terms-privacy

Copyright © by SIAM. Unauthorized reproduction of this article is prohibited.

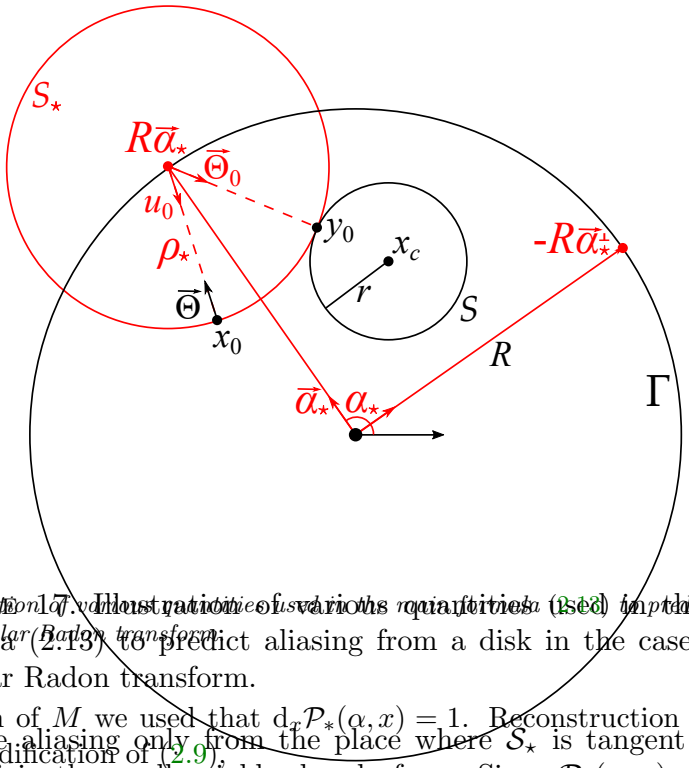

Figure 17. Illustration of various quantities used in the main formula (2.13) to predict aliasing from a disk in the case of the circular Radon transform.

To illustrate aliasing only from the place where $S_\star$ is tangent to S we select Ω to be a sufficiently small neighborhood of $\alpha_\star$. Since $\mathcal{P}_*(\alpha,x)=|x-R\vec{\alpha}|$ and $\mathcal{P}(\alpha)=|x_c-R\vec{\alpha}|-r$, we find

$$u_0=\frac{x_0-R\vec{\alpha}_\star}{|x_0-R\vec{\alpha}_\star|},\tag{5.8}$$

$$u_0=-R\vec{\alpha}_\star\cdot(u_0-\vec{\Theta}_0)=-(R/\rho_\star)\vec{\alpha}_\star\cdot(x_0-y_0),$$

see Figure 17.

For reconstructions we use

$$R=5,\quad r=1,\quad x_c=(1,1),\quad (\alpha_-,\alpha_+)=(0.53\pi,2.24),\quad w_\Omega=(1.42,2.95),\tag{5.11}$$

$$\Omega=[\alpha_\star-\pi/4,\alpha_\star+\pi/4].$$

In the first reconstruction, $\epsilon=10^{-2}$, $N_\alpha=500$ and in the second – $\epsilon=0.5\cdot10^{-2}$, $N_\alpha=1000$. The results are shown in Figures 18 and 19, respectively. The left panels show the limited angle reconstruction of the region $|x_1|,|x_2|\le4$. The middle panels show the limited angle reconstruction of an ROI. The ROI is a small square centered at x_0 with side length 40ϵ, the ROI is shown on the left panel. The right panels show the profiles of the reconstructed difference $\epsilon^{-1/2}(f_\epsilon^{\rm rec}(x)-f_\epsilon^{\rm rec}(x_0))$ along the line segment $x=x_0+t\vec{\Theta}_0$, $|t|\le6$, shown in the middle panel. To be specific, we select a "+" in (5.9), i.e. $\rho_\star$ satisfies $|x_c-R\vec{\alpha}_\star|=r+\rho_\star$. This implies that $M=(1/r)+(1/\rho_\star)$ and $\vec{\Theta}_0=(y_0-R\vec{\alpha}_\star)/|y_0-R\vec{\alpha}_\star|$ points towards the center of curvature of S at y_0 (see Figure 17). Similarly to the CRT, our construction ensures that $S_{\alpha_\star,\rho_\star+\delta}$, where $0<\delta\ll1$, intersects S at two points.

$$f_\epsilon^{\rm rec}(x)=-\frac{\Delta\alpha}{2\pi}\sum_{\alpha_k\in\Omega}\frac{1}{\epsilon}\int\frac{\partial_\rho\hat f_\epsilon(\alpha_k,\rho)}{p-\mathcal{P}_*(x,\alpha_k)}\mathrm{d}\rho,\tag{5.10}$$

$$\hat f(\alpha_k,\rho)=\int w_\epsilon(\rho-\rho')\hat f(\alpha_k,\rho')\mathrm{d}\rho',\quad \alpha_k=(2\pi/N_\alpha)k,\quad w(\rho)=(15/16)(1-\rho^2)_+^2,$$

i.e., w is the same as in (4.7). Clearly, the reconstruction is not theoretically exact anymore. But it preserves the strength of the singularities (in the Sobolev scale). Again, the weights in both the Radon transform and the inversion formula are set to 1: $W(\alpha,\rho,x)=1$, $w(\alpha,x)\equiv1$.

The function f is the characteristic function of the disk centered at x_c with radius r. Thus, $\mathcal{S}=\{x\in\mathbb{R}^2:|x-x_c|=r\}$; see Figure 17.

At a given x_0, aliasing arises due to the parts of $\mathcal{S}$ where various $\mathcal{S}_{\alpha,\rho}\ni x_0$ are tangent to $\mathcal{S}$. All such (α,ρ) are found by solving each of the two equations

$$|x_c-R\vec{\alpha}|-|x_0-R\vec{\alpha}|=\pm r\tag{5.9}$$

for α and setting $\rho=|x_0-R\vec{\alpha}|$. Generally, up to four solutions (α,ρ) (i.e., up to four circles $\mathcal{S}_{\alpha,\rho}$) can exist. To simplify the experiment, we reverse the argument. We pick some pair $(\alpha_\star,\rho_\star)$ such that $\mathcal{S}_\star$ is tangent to $\mathcal{S}$ at some y_0 and then select some $x_0\in\mathcal{S}_\star$. To be specific, we select a "+" in (5.9), i.e. $\rho_\star$ satisfies $|x_c-R\vec{\alpha}_\star|=r+\rho_\star$. This implies that $M=(1/r)+(1/\rho_\star)$ and $\vec{\Theta}_0=(y_0-R\vec{\alpha}_\star)/|y_0-R\vec{\alpha}_\star|$ points towards the center of curvature of $\mathcal{S}$ at y_0 (see Figure 17). Similarly to the CRT, our construction ensures that $\mathcal{S}_{\alpha_\star,\rho_\star+\delta}$, where $0<\delta\ll1$, intersects $\mathcal{S}$ at two points.

Downloaded 09/12/24 to 5.198.137.25 . Redistribution subject to SIAM license or copyright; see https://epubs.siam.org/terms-privacy

Copyright © by SIAM. Unauthorized reproduction of this article is prohibited.

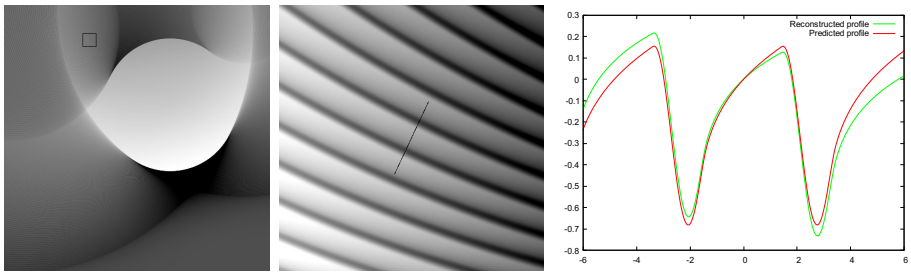

Figure 18. *Disk phantom, limited angle GRT reconstruction: $\epsilon = 0.01$, $N_\alpha = 500$. Left: global reconstruction; middle: reconstruction inside the square ROI shown on the left; right: profiles of the reconstruction (green) and prediction (red) along the line segment $x = x_0 + \epsilon h\vec{\Theta}$, $|h| \le 6$, shown in the middle. The variable h is on the horizontal axis.*

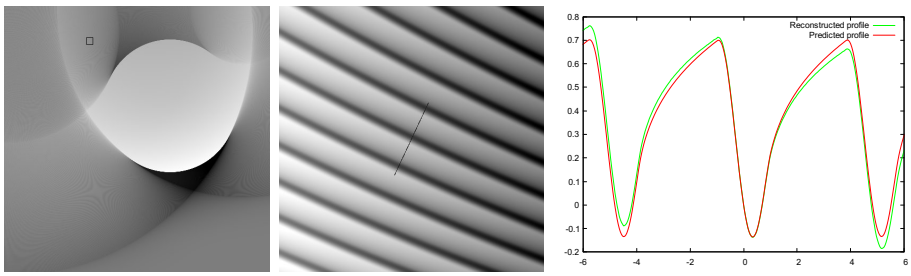

Figure 19. *Disk phantom, limited angle GRT reconstruction: $\epsilon = 0.005$, $N_\alpha = 1000$. Left: global reconstruction; middle: reconstruction inside the square ROI shown on the left; right: profiles of the reconstruction (green) and prediction (red) along the line segment $x = x_0 + \epsilon h\vec{\Theta}$, $|h| \le 6$, shown in the middle. The variable h is on the horizontal axis.*

To illustrate aliasing only from the place where $\mathcal{S}_\star$ is tangent to $\mathcal{S}$ we select Ω to be a sufficiently small neighborhood of $\alpha_\star$. Since $\mathcal{P}_*(\alpha, x) = |x - R\vec{\alpha}|$ and $\mathcal{P}(\alpha) = |x_c - R\vec{\alpha}| - r$, we find

$$
\begin{aligned}
u_0 &= \frac{x_0 - R\vec{\alpha}_\star}{|x_0 - R\vec{\alpha}_\star|}, \\
\mu_0 &= -R\vec{\alpha}_\star^{\perp} \cdot (u_0 - \vec{\Theta}_0) = -(R/\rho_\star)\vec{\alpha}_\star \cdot (x_0 - y_0);
\end{aligned}
\tag{5.10}
$$

see Figure 17.

For reconstructions we use

$$
\begin{aligned}
&R = 5,\ x_c = (1,1),\ r = 2,\ (\alpha_\star, \rho_\star) = (0.53\pi, 2.24),\ x_0 = (-1.42, 2.95), \\
&\Omega := [\alpha_\star - \pi/4, \alpha_\star + \pi/4].
\end{aligned}
\tag{5.11}
$$

In the first reconstruction, $\epsilon = 10^{-2}$, $N_\alpha = 500$ and in the second – $\epsilon = 0.5 \cdot 10^{-2}$, $N_\alpha = 1000$. The results are shown in Figures 18 and 19, respectively. The left panels show the limited angle reconstruction of the region $|x_1|, |x_2| \le 4$. The middle panels show the limited angle reconstruction of an ROI. The ROI is a small square centered at x_0 with side length 40ϵ; the ROI is shown on the left panel. The right panels show the profiles of the reconstructed difference $\epsilon^{-1/2}(f_\epsilon^{\mathrm{rec}}(x) - f_\epsilon^{\mathrm{rec}}(x_0))$ (green) and the prediction given by the main term on the

Downloaded 09/12/24 to 5.198.137.25 . Redistribution subject to SIAM license or copyright; see https://epubs.siam.org/terms-privacy

Copyright © by SIAM. Unauthorized reproduction of this article is prohibited.

right in (2.13) (red) along the line segment $x = x_0 + \epsilon h\vec{\Theta}$, $|h| \leq 6$, shown in the middle panel. The values of h are on the horizontal axis of the profiles. The unit vector $\vec{\Theta}$ is chosen to be orthogonal to $\mathcal{S}_\star$ at x_0 (i.e., $\vec{\Theta}$ and u_0 are parallel; see Figure 17). In the experiments we set $\vec{\Theta} = -u_0$. As is seen, reducing ϵ and $\Delta\alpha$ improves the match between the reconstruction and prediction.

Appendix A. Proofs of lemmas.

A.1. Proof of Lemma 2.2. The property $\mathcal{P}(\alpha_\star) = p_\star$ follows from assumption 2.1(2). Recall that $H(y) = 0$ is a local equation of $\mathcal{S}$ (cf. (2.2) and the paragraph preceding it). To find $\mathcal{P}(\alpha)$, we solve

$$H(y) = 0, \ \lambda \mathrm{d}H(y) = \mathrm{d}_y \mathcal{P}_*(\alpha, y) \tag{A.1}$$

for $y \in \mathcal{S}$ and λ in terms of α near $(\lambda = 1, y = y_0, \alpha = \alpha_\star)$ and then set $\mathcal{P}(\alpha) = \mathcal{P}_*(\alpha, y(\alpha))$. Assumptions 2.1(1), 2.1(2), 2.1(4) and the implicit function theorem imply that $y(\alpha)$ and, therefore, $\mathcal{P}(\alpha)$ are smooth in a small neighborhood $\Omega \ni \alpha_\star$. Since $y'(\alpha)$ is tangent to $\mathcal{S}$, using the second equation in (A.1) gives $\mathcal{P}'(\alpha_\star) = \partial_\alpha \mathcal{P}_*(\alpha_\star, y_0)$.

A.2. Proof of Lemma 3.1. Denote

$$H(x, \alpha, \epsilon) := \frac{\mathcal{P}_*(\alpha, x) - \mathcal{P}(\alpha)}{\epsilon}, \ x = x_0 + \epsilon\check{x}, \alpha \in \Omega. \tag{A.2}$$

Since $\mu_0 \neq 0$ (cf. (2.6)), we have $|\mathcal{P}_*(\alpha, x_0) - \mathcal{P}(\alpha)| \geq c|\alpha - \alpha_\star|$ for any $\alpha \in \Omega$ and some $c > 0$. Hence

$$|H(x, \alpha_k, \epsilon)| \geq c_1|k - k_\star| \text{ for all } |\check{x}| \leq c, \alpha_k \in \Omega, |k - k_\star| \geq c_2, \tag{A.3}$$

for some $c, c_1, c_2 > 0$ and all $\epsilon > 0$ sufficiently small. From (3.5),

$$\begin{aligned} &f_\epsilon^{\text{rec-1}}(x_0 + \epsilon\check{x}) - f_\epsilon^{\text{rec-1}}(x_0) = -\frac{\Delta\alpha}{2\pi\epsilon^{1/2}}(J + O(\epsilon^{1/2})), \\ &J := \sum_{\alpha_k \in \Omega} \omega(\alpha_k, x_0)\varphi_1(\alpha_k)\left[\psi\left(H(x_0 + \epsilon\check{x}, \alpha_k, \epsilon)\right) - \psi\left(H(x_0, \alpha_k, \epsilon)\right)\right]. \end{aligned} \tag{A.4}$$

The $O(\epsilon^{1/2})$ term in parentheses on the right in (A.4) denotes the contribution, which arises due to the x-dependence of ω in (3.5). Here we use (3.6) with $n = 0$, (A.3), and that for some c and all $\check{x}$ in a bounded set,

$$|\omega(\alpha, x_0 + \epsilon\check{x}) - \omega(\alpha, x_0)| \leq c\epsilon, \ |\varphi_1(\alpha)| \leq c, \ \alpha \in \Omega, \tag{A.5}$$

hence

$$O(\epsilon)\left(O(1) + \sum_{c_2 \leq |k - k_\star| \leq O(1/\epsilon)} |k - k_\star|^{-1/2}\right) = O(\epsilon^{1/2}). \tag{A.6}$$

From (2.6),

$$\begin{aligned} H(x_0 + \epsilon\check{x}, \alpha, \epsilon) &= H(x_0, \alpha, \epsilon) + \mathrm{d}_x \mathcal{P}_*(\alpha, x_0)\check{x} + O(\epsilon) \\ &= H(x_0, \alpha, \epsilon) + u_0 \cdot \check{x} + O(\epsilon + |\alpha - \alpha_\star|). \end{aligned} \tag{A.7}$$

Downloaded 09/12/24 to 5.198.137.25 . Redistribution subject to SIAM license or copyright; see https://epubs.siam.org/terms-privacy

Copyright © by SIAM. Unauthorized reproduction of this article is prohibited.

Also, $|\omega(x_0,\alpha)\varphi_1(\alpha)| \le c$ for some c and all $\alpha \in \Omega$. Therefore, by (3.6) with $n=1$ and (A.3),

$$\begin{aligned}
&\sum_{\alpha_k\in\Omega} \omega(\alpha_k,x_0)\varphi_1(\alpha_k)[\psi(H(x_0+\epsilon\check{x},\alpha_k,\epsilon)) - \psi(H(x_0,\alpha_k,\epsilon)+u_0\cdot\check{x})] \\
&\quad = \sum_{|k|\le O(1/\epsilon)} \psi'(H(x_0,\alpha_k,\epsilon)+O(1))O(\epsilon+\epsilon|k-k_\star|) \\
&\quad = O(\epsilon)\left(1+\sum_{c_2\le|k-k_\star|\le O(1/\epsilon)} \frac{1+|k-k_\star|}{|k-k_\star|^{3/2}}\right) = O(\epsilon^{1/2}).
\end{aligned} \tag{A.8}$$

Here we use that $w' \in L^q(\mathbb{R})$, $q>2$ (see assumption 2.4(1)), so ψ' is continuous. This shows that if w does not have the required smoothness (e.g., if w is the characteristic function of a detector pixel), the magnitude of the expression in (A.8) may turn out to be much larger, leading to a slower rate of convergence in Theorem 2.5 (or even to a breakdown of the convergence altogether).

From (A.4), (A.7), and (A.8),

$$\begin{aligned}
&J = \sum_{\alpha_k\in\Omega} \omega(\alpha_k,x_0)\varphi_1(\alpha_k)\Delta\psi(H(x_0,\alpha_k,\epsilon)) + O(\epsilon^{1/2}), \\
&\Delta\psi(t) := \psi(t+u_0\cdot\check{x}) - \psi(t).
\end{aligned} \tag{A.9}$$

Furthermore,

$$H(x_0,\alpha_k,\epsilon) = \mu_0\frac{\alpha_k-\alpha_\star}{\epsilon} + R_k,\ \ R_k = O(\epsilon(k-k_\star)^2). \tag{A.10}$$

Denote, for simplicity, $a_k = \mu_0\kappa(k-k_\star)$. Then

$$\Delta\psi(a_k+R_k) - \Delta\psi(a_k) = R_k\Delta\psi'(a_k+\xi_k), \tag{A.11}$$

where $|\xi_k| \le |R_k|$. We can assume that Ω is sufficiently small, so that

$$|\mu_0(\alpha_k-\alpha_\star)+\epsilon R_k| \ge c|\alpha_k-\alpha_\star| \ \ \forall \alpha_k\in\Omega \tag{A.12}$$

for some $c>0$. Dividing by ϵ implies

$$|a_k+R_k| \ge c\kappa|k-k_\star| \ \ \forall \alpha_k\in\Omega \tag{A.13}$$

with the same c. Using (3.6) with $n=2$ gives

$$\begin{aligned}
&\sum_{c\le|k-k_\star|\le O(1/\epsilon)} \omega(\alpha_k,x_0)\varphi_1(\alpha_k)[\Delta\psi(a_k+R_k)-\Delta\psi(a_k)] \\
&\quad = \sum_{c\le|k-k_\star|\le O(1/\epsilon)} \frac{O(\epsilon|k-k_\star|^2)}{1+|k-k_\star|^{5/2}} = O(\epsilon^{1/2})
\end{aligned} \tag{A.14}$$

for some $c>0$ sufficiently large. The requirement $|k-k_\star| \ge c$ is needed, because $\psi''(\hat{q})$, on which the estimate (A.14) is based, may not exist for $\hat{q}$ in a compact set when $w' \in L^q$.

Downloaded 09/12/24 to 5.198.137.25 . Redistribution subject to SIAM license or copyright; see https://epubs.siam.org/terms-privacy

Copyright © by SIAM. Unauthorized reproduction of this article is prohibited.

To estimate the remaining finitely many terms without appealing to the second derivative we write

$$\begin{aligned}&\Delta\psi(a_k+R_k)-\Delta\psi(a_k)\\&=[\psi(a_k+u_0\cdot\check{x}+R_k)-\psi(a_k+u_0\cdot\check{x})]-[\psi(a_k+R_k)-\psi(a_k)]\\&=O(\epsilon),\ |k-k_\star|\le c.\end{aligned}\tag{A.15}$$

This follows, because ψ' is continuous on all of $\mathbb{R}$ and $R_k=O(\epsilon)$ whenever $|k-k_\star|\le c$ (cf. (A.10)). This is another place where we use that $w'\in L^q$. If w is not sufficiently smooth, the quantity in (A.15) may turn out to be much larger.

It is clear that all the big-O terms are uniform with respect to $\check{x}$ (and, hence, h) restricted to a bounded set. Combining (A.4), (A.9), (A.14), and (A.15) finishes the proof.

A.3. Proof of Lemma 3.2. Denote

$$J:=\int s^{-1}\left[\varphi_3'(s+q+\Delta q)-\varphi_3'(s+q)\right]\mathrm{d}s,\tag{A.16}$$

where we omitted the dependence on α for simplicity. All the big-O terms in this subsection are uniform with respect to $\alpha\in\Omega$. Restricting the integral in (A.16) to $|s|\le 1$ we find

$$J_1:=\int_{|s|\le 1}s^{-1}\left(\left[\varphi_3'(s+q+\Delta q)-\varphi_3'(q+\Delta q)\right]-\left[\varphi_3'(s+q)-\varphi_3'(q)\right]\right)\mathrm{d}s.\tag{A.17}$$

Clearly, $J_1=O(|\Delta q|)$ uniformly in $|q|\le c$. Here we have used that φ_3 is smooth, so its third order derivative is bounded on compact sets. By (3.18), $\varphi_3''(p)=O(|p|^{-3/2})$, $p\to\infty$. Hence

$$J_2:=\int_{|s|\ge 1}s^{-1}\left[\varphi_3'(s+q+\Delta q)-\varphi_3'(s+q)\right]\mathrm{d}s=O(|\Delta q|)\tag{A.18}$$

uniformly in $|q|\le c$. Combining the estimates for $J_{1,2}$ proves the lemma.

A.4. Proof of Lemma 4.4. The Euler–MacLauren formula reads as follows [37, equation (25.7)]:

$$\begin{aligned}\sum_{k=a}^{b-1}f(k)=&\int_a^b f(t)\mathrm{d}t+\sum_{m=1}^{N'}\frac{b_m}{m!}(f^{(m-1)}(b)-f^{(m-1)}(a))\\&-\int_a^b\frac{B_{N'}(\{1-t\})}{N'!}f^{(N')}(t)\mathrm{d}t.\end{aligned}\tag{A.19}$$

Here $b>a$ are integers, B_m and b_m are Bernoulli polynomials and numbers, respectively, $\{t\}=t-\lfloor t\rfloor$ is the fractional part of $t\in\mathbb{R}$, and $\lfloor t\rfloor$ is the floor function, i.e., the largest integer not exceeding t.

Substituting $f(t)=g(\epsilon t)$, taking the limit as $a\to-\infty$, $b\to\infty$ (which is allowed due to the decay of g and its derivatives), changing variables $\tau=\epsilon t$, and using that $g^{(N')}\in L^1(\mathbb{R})$, we finish the proof.

Copyright © by SIAM. Unauthorized reproduction of this article is prohibited.

Downloaded 09/12/24 to 5.198.137.25 . Redistribution subject to SIAM license or copyright; see https://epubs.siam.org/terms-privacy

Acknowledgment. The author thanks the anonymous reviewers whose comments helped improve the manuscript.

REFERENCES

[1] C. L. Epstein, *Introduction to the Mathematics of Medical Imaging*, 2nd ed., SIAM, Philadelphia, 2008.
[2] B. Li, G. B. Avinash, and J. Hsieh, *Resolution and noise trade-off analysis for volumetric CT*, Med. Phys., 34 (2007), pp. 3732–3738.
[3] R. Grimmer, J. Krause, M. Karolczak, R. Lapp, and M. Kachelriess, *Assessment of spatial resolution in CT*, in IEEE Nuclear Science Symposium Conference Record, IEEE, Piscataway, NJ, 2008, pp. 5562–5566.
[4] S. N. Friedman, G. S. Fung, J. H. Siewerdsen, and B. M. Tsui, *A simple approach to measure computed tomography (CT) modulation transfer function (MTF) and noise-power spectrum (NPS) using the American College of Radiology (ACR) accreditation phantom*, Med. Phys., 40 (2013), pp. 1–9.
[5] H. Kruse, *Resolution of reconstruction methods in computerized tomography*, SIAM J. Sci. Stat. Comput., 10 (1989), pp. 447–474.
[6] L. Desbat, *Efficient sampling on coarse grids in tomography*, Inverse Problems, 9 (1993), pp. 251–269.
[7] F. Natterer, *Sampling in fan beam tomography*, SIAM J. Appl. Math., 53 (1993), pp. 358–380.
[8] F. Natterer, *Sampling and resolution in CT*, in Proceedings of the Fourth International Symposium (CT-93), Novosibirsk, 1993, M. M. Lavrentév, ed., VSP, Utrecht, Netherlands, 1995, pp. 343–354.
[9] V. P. Palamodov, *Localization of harmonic decomposition of the Radon transform*, Inverse Problems, 11 (1995), pp. 1025–1030.
[10] A. Caponnetto and M. Bertero, *Tomography with a finite set of projections: Singular value decomposition and resolution*, IEEE Trans. Inform. Theory, 13 (1997), pp. 1191–1205.
[11] A. Faridani and E. Ritman, *High-resolution computed tomography from efficient sampling*, Inverse Problems, 16 (2000), pp. 635–650.
[12] A. Faridani, *Sampling theory and parallel-beam tomography*, in Sampling, Wavelets, and Tomography, Appl Numer. Harmon. Anal. 63, Birkhäuser Boston, Boston, MA, 2004, pp. 225–254.
[13] A. Rieder and A. Schneck, *Optimality of the fully discrete filtered backprojection algorithm for tomographic inversion*, Numer. Math., 108 (2007), pp. 151–175.
[14] S. H. Izen, *Sampling in flat detector fan beam tomography*, SIAM J. Appl. Math., 72 (2012), pp. 61–84.
[15] P. Stefanov, *Semiclassical sampling and discretization of certain linear inverse problems*, SIAM J. Math. Anal., 52 (2020), pp. 5554–5597.
[16] F. Monard and P. Stefanov, *Sampling the x-ray transform on simple surfaces*, SIAM J. Math. Anal., 53 (2023), pp. 1707–1736.
[17] P. Stefanov, *The Radon transform with finitely many angles*, Inverse Problems, 39 (2023), 105003.
[18] A. Katsevich, *A local approach to resolution analysis of image reconstruction in tomography*, SIAM J. Appl. Math., 77 (2017), pp. 1706–1732.
[19] A. Katsevich, *Analysis of reconstruction from discrete Radon transform data in $\mathbb{R}^3$ when the function has jump discontinuities*, SIAM J. Appl. Math., 79 (2019), pp. 1607–1626.
[20] A. Katsevich, *Analysis of resolution of tomographic-type reconstruction from discrete data for a class of distributions*, Inverse Problems, 36 (2020), 124008.
[21] A. Katsevich, *Resolution analysis of inverting the generalized Radon transform from discrete data in $\mathbb{R}^3$*, SIAM J. Math. Anal., 52 (2020), pp. 3990–4021.
[22] A. Katsevich, *Resolution analysis of inverting the generalized N-dimensional Radon transform in $\mathbb{R}^n$ from discrete data*, J. Fourier Anal. Appl., 29 (2023), 6.
[23] A. Katsevich, *Novel resolution analysis for the Radon transform in $\mathbb{R}^2$ for functions with rough edges*, SIAM J. Math. Anal., 55 (2023), pp. 4255–4296.
[24] P. M. Joseph and R. A. Schulz, *View sampling requirements in fan beam computed tomography*, Med. Phys., 7 (1980), pp. 692–702.

Downloaded 09/12/24 to 5.198.137.25 . Redistribution subject to SIAM license or copyright; see https://epubs.siam.org/terms-privacy

Copyright © by SIAM. Unauthorized reproduction of this article is prohibited.

[25] P. Kuchment, *Generalized transforms of Radon type and their applications*, in The Radon Transform, Inverse Problems, and Tomography, G. Ólafsson and E. T. Quinto, eds., American Mathematical Society, Providence, RI, 2005, pp. 67–91.
[26] G. Ambartsoumian and E. T. Quinto, *Generalized Radon transforms and applications in tomography*, Inverse Problems, 36 (2020), 020301.
[27] F. Natterer, *The Mathematics of Computerized Tomography*, Classics Appl. Math. 32, SIAM, Philadelphia, 2001.
[28] G. Beylkin, *The Inversion Problem and Applications of the Generalized Radon Transform*, Ft. Belvoir Defense Technical Information Center, Fairfax, VA, 1984.
[29] A. Katsevich, *An accurate approximate algorithm for motion compensation in two-dimensional tomography*, Inverse Problems, 26 (2010), 065007.
[30] E. T. Quinto, *The dependence of the generalized Radon transforms on defining measures*, Trans. Amer. Math. Soc., 257 (1980), pp. 331–346.
[31] A. G. Ramm and A. I. Zaslavsky, *Singularities of the Radon transform*, Bull. Amer. Math. Soc., 25 (1993), pp. 109–115.
[32] A. G. Ramm and A. I. Zaslavsky, *Reconstructing singularities of a function given its Radon transform*, Math. Comput. Model., 18 (1993), pp. 109–138.
[33] N. I. Muskhelishvili, *Singular Integral Equations, Boundary Problems of Functions Theory and Their Applications to Mathematical Physics*, Springer, Dordrecht, Netherlands, 1958.
[34] W. Rudin, *Real and Complex Analysis*, McGraw-Hill, London, 1970.
[35] F. D. Gakhov, *Boundary Value Problems*, Pergamon Press, Oxford, 1966.
[36] A. P. Prudnikov, Y. A. Brychkov, and O. I. Marichev, *Integrals and Series*, *Vol.* 1, *Elementary Functions*, Gordon and Breach, New York, 1986.
[37] V. Kac and P. Cheung, *Quantum Calculus*, Springer, New York, 2002.
[38] G. Nemes, *Error bounds for the asymptotic expansion of the Hurwitz zeta function*, Proc. R. Soc. Ser. A Math. Phys. Eng. Sci., 473 (2017), 20170363.

Downloaded 09/12/24 to 5.198.137.25 . Redistribution subject to SIAM license or copyright; see https://epubs.siam.org/terms-privacy

Copyright © by SIAM. Unauthorized reproduction of this article is prohibited.